

A fibril-scale viscohyperelastic model for the mechanics of vocal-fold tissues

Alberto Terzolo¹, Lucie Bailly^{1,*} and Laurent Orgéas¹

¹Univ. Grenoble Alpes, CNRS, Grenoble INP, 3SR, 38000 Grenoble, France

Correspondence*:

lucie.bailly@3sr-grenoble.fr

2 ABSTRACT

3 Modeling the mechanics of human vocal folds during phonation is still a challenging task. This
4 is partly due to the mechanics of their soft and highly anisotropic fibrous tissues, which can
5 undergo finite strains with both elasticity and strain rate sensitivity. In this study, we propose a
6 visco-hyperelastic micro-mechanical model capable of predicting the complex cyclic response of
7 the vocal-fold fibrous tissues based on their histo-mechanical properties. For that purpose, we
8 start from the hyperelastic micro-mechanical model proposed in [Terzolo *et al.*, *J Mech Behavior*
9 *Biomed Mater* 128 (2022)]. We include in the model non-linear viscoelastic contributions at the
10 fibril scale to account for the dissipative and time-dependent response of vocal fold tissues. The
11 relevance of the model is demonstrated and discussed through comparison with a comprehensive
12 set of reference experimental data, within a wide range of loading modes, strains, and strain
13 rates: cyclic and multiaxial loadings at finite strains (tension, compression and shear); small
14 (SAOS) and large (LAOS) amplitude oscillatory shear from low to high frequencies. This study
15 elucidates how the viscoelasticity of vocal-fold tissues can result from combined time-dependent
16 micro-mechanisms, such as the kinematics and the deformation of their fibril bundles, as well
17 as the mechanical interactions likely to develop among fibrils and the surrounding amorphous
18 matrix.

19 **Keywords:** Vocal folds, Fibril, 3D microstructure, Multiscale mechanical modeling, Viscoelasticity, Multiaxial loadings, SAOS, LAOS

1 INTRODUCTION

20 Human vocal folds are soft laryngeal structures with remarkable mechanical properties. During phonation,
21 the vocal folds deform under the action of pulmonary airflow and laryngeal motions, sustaining vibrations
22 in a wide range of amplitudes, frequencies (from 50 Hz to over 1500 Hz), and degrees of collisions.
23 These multiple configurations involve complex and coupled multiaxial mechanical stresses (in tension,
24 compression and shear), that the tissues can withstand upon finite strains at various strain rates (Miri, 2014;
25 Vampola *et al.*, 2016). These properties are inherited from the composite and hierarchical structure of the
26 vocal folds and surrounding laryngeal muscles. More specifically, the vocal folds are made up of two main
27 load-bearing layers: the *lamina propria*, *i.e.*, a loose connective tissue, and the *vocalis* muscle. Both layers
28 are composed of networks of collagen, elastin and/or skeletal muscle microfibrils, embedded in a soft
29 hydrogel-like matrix (Fig. 1; Hirano (1974); Benboujja and Hartnick (2021); Ferri-Angulo *et al.* (2023)).
30 However, to date, our knowledge is still not sufficient to understand the relationship between the fibril-scale
31 architecture of vocal folds and their macroscale (tissue-scale) time-dependent performances.

This is mainly ascribed to the difficulty to characterize the vocal folds mechanics at high physiological strain rates. Although recent progress has been made in time-resolved 3D microimaging of fast-vibrating structures (Klos et al., 2024), to date, characterization of the mechanical behavior of vocal-fold tissues at high frequencies (e.g., from 100 Hz to 1 kHz) is still limited to the macroscale. High-speed videostroboscopy used in clinical voice assessment enabled the quantification of the time-decay of vocal-fold vibrations at phonation offset (DeJonckere and Lebacq, 2020; Radolf et al., 2022), and of resonance properties by external excitation of the larynx (Švec et al., 2000). Such *in vivo* approaches allowed to measure an average damping ratio $\zeta \approx 0.07\text{--}0.20$, describing the dissipation of stored energy in oscillations for frequencies between 100 and 200 Hz (Švec et al., 2000; DeJonckere and Lebacq, 2020; Radolf et al., 2022), and which partly arises from the viscoelastic behavior of the tissues. The time-dependent mechanical properties of vocal-fold tissues have also been demonstrated *ex vivo* by numerous phenomena, including strain-rate sensitivity of stress-strain behavior, creep, stress relaxation, stress hysteresis and related accommodation upon cycling, with the magnitude of the hysteresis loop dependent on strain rate (Kelleher et al., 2013a; Chan and Titze, 1999, 2000; Chan, 2004; Klemuk and Titze, 2004; Titze et al., 2004; Chan and Rodriguez, 2008; Miri et al., 2014; Chan, 2018; Cochereau et al., 2020). Viscoelastic properties of excised *lamina propria* samples were mostly studied using standard shear Dynamic Mechanical Analysis (DMA), also called Small-Amplitude Oscillatory Shear (SAOS), *i.e.*, within the linear regime (Chan and Titze, 1999, 2000; Chan, 2004; Klemuk and Titze, 2004; Titze et al., 2004; Chan and Rodriguez, 2008). Such works allowed to characterize the shear storage G' and loss G'' moduli of the vocal-fold “cover” (*i.e.*, superficial sublayer of the *lamina propria* combined with the *epithelium* that covers it) for excitation frequencies f up to 250 Hz. Thereby, these dynamic moduli increase (resp. decrease) with the applied frequency (resp. strain), while the loss factor ($\tan \delta = \zeta^* = G''/G'$; Dashatan et al. (2023); Koruk and Rajagopal (2024)) decreases monotonically with frequency, down to a mean value of 0.73 for f within 100–250 Hz (Chan and Rodriguez, 2008). Such experiments were recently extended to Large-Amplitude Oscillatory Shear (LAOS), showing that *lamina propria* sublayers experience intercycle strain softening during oscillatory strain sweeps, intracycle strain stiffening, shear thinning while increasing the shear rate, as well as complex stress hysteresis that depends on the applied strain and strain rate (Chan, 2018).

To better analyze these data and unveil the underlying mechanisms, several theoretical approaches were adopted. Some phenomenological approaches were first developed (Zhang et al., 2006, 2007, 2009). However, the constitutive parameters of these models can hardly be related to relevant histological descriptors of the vocal tissues. Since 2010, a few authors have purposely proposed micromechanical models including the architecture of vocal tissues to open a new insight into voice biomechanics. Two modeling routes have been adopted:

(i) Poroelastic formulations have been developed to describe the fluid/solid phases of vocal tissues and to predict their dynamics (Miri et al., 2014; Tao et al., 2009; Scholp et al., 2020). However, such approaches rely on parameters which are still lacking experimental measurements (*e.g.*, permeability, *in situ* observations of fluid dynamics, *etc.*).

(ii) Other authors have idealized the architecture of the fibrous networks of the *lamina propria* and the *vocalis* (*e.g.*, using structural descriptors such as the fibril volume fraction, diameter, preferred orientations, *etc.*) to derive their mechanical contribution from microstructural and/or micromechanical measurements (Miri et al., 2013; Kelleher et al., 2013b; Terzolo et al., 2022). This enabled the identification of the strain-induced micromechanisms (*e.g.*, progressive elongation and reorientation of collagen fibrils and myofibrils, mechanical interactions between microconstituents, *etc.*) which modulate the nonlinear and anisotropic macroscale behavior of vocal tissues (Terzolo et al., 2022). However, these micromechanical

76 formulations have been developed within a general hyperelastic framework, thus neglecting the important
 77 dissipative and time-dependent mechanisms likely to develop during the vibrations of vocal tissues.

78 Therefore, this work aims at providing a multi-scale mechanical model able to reproduce the non-linear
 79 macroscopic visco-hyperelastic mechanical behavior of the vocal fold layers (*i.e.*, *lamina propria*, *vocalis*)
 80 from low to high frequency and strains, from the knowledge of their architecture and mechanics at the
 81 fibril scale. To do so, we introduce microstructural time-dependent effects to the hyperelastic formulation
 82 developed in Terzolo et al. (2022). Based on histological and biomechanical data available in the literature
 83 and covering a wide range of loading modes, strain levels and rates, the model suitability to predict the
 84 time-dependent multiscale mechanics of the vocal-fold layers is highlighted and discussed.

2 FORMULATION OF THE MICRO-MECHANICAL MODEL

85 2.1 Structural assumptions

86 The structural assumptions of the model are identical to those reported in Terzolo et al. (2022). Briefly,
 87 both the *lamina propria* and the *vocalis* are considered as incompressible composite materials made of a
 88 gel-like matrix (composed of cells, elastin, gel-like ground substance for the *lamina propria* and elastin,
 89 proteoglycans, glycoproteins for the *vocalis*) reinforced by a network of connected and orientated fibril
 90 bundles (Fig. 1):

- 91 • For the *lamina propria* (Fig. 1a, case ①), each fibril bundle is seen as an assembly of parallel collagen
 92 fibrils of initial diameter d_0 , length ℓ_o^f , and tortuosity $\xi_0 = \ell_0^f/\ell_0$, ℓ_0 being their initial chord length. They
 93 are characterized by a waviness of about 10 monomodal sinusoids between nodes, with a wave amplitude
 94 R_0 and a spatial periodicity H_0 , so that $\ell_0 \approx 10 H_0$ at rest.
- 95 • For the *vocalis* (Fig. 1a, case ②), each fibril bundle is seen as an assembly of parallel myofibrils (of
 96 initial diameter d_{0m} , tortuosity ξ_{0m} , wave amplitude R_{0m} , spatial periodicity H_{0m} , and chord length
 97 $\ell_0 \approx 10H_{0m}$), surrounded by a sheath of collagen fibrils (of initial diameter d_{0c} , tortuosity ξ_{0c} , wave
 98 amplitude R_{0c} , spatial periodicity H_{0c}).
- 99 • The fibrous architecture of the *lamina propria* exhibits a collagen fibril content Φ (yielding to n_f
 100 collagen fibrils in Fig. 1a), whereas the *vocalis* displays a collagen fibril content Φ_c and a myofibril
 101 content Φ_m (yielding to n_{fc} collagen fibrils and n_{fm} myofibrils). Both tissues are idealized as networks
 102 of connected fibril bundles. These networks are built from the periodic repetition of a representative
 103 elementary volume (REV), composed of 4 fibril bundles connected to a central node C_0 , and to the 4
 104 nodes C_i , of corresponding neighboring REVs at their extremities (Fig. 1b). At rest, each fibril bundle
 105 i is also characterized by its initial mean orientation \mathbf{E}_i as depicted in Fig. 1b. This set of orientation
 106 directors introduces structural anisotropy. The distances between node C_0 and its unconnected neighbors
 107 C_q (see dotted lines in Fig. 1b), *i.e.*, along the initial directions $\mathbf{E}_q = C_0C_q/\|C_0C_q\|$, are noted δ_q .

108 2.2 Micromechanical assumptions

109 *Kinematics* – When subjected to a macroscopic transformation gradient \mathbf{F} and a macroscopic velocity
 110 gradient \mathbf{L} , the tissue REVs deform from their initial configuration to a deformed one. As a consequence,
 111 fibril bundles (un)fold so that their chord length is $\ell_i = \ell_0\|\mathbf{F} \cdot \mathbf{E}_i\|$ in the deformed configuration, *i.e.*, with
 112 a tensile stretch and strain $\lambda_i = \ell_i/\ell_0$ and $\varepsilon_i = \ln \lambda_i$, respectively. This process occurs at a tensile strain
 113 rate $\dot{\varepsilon}_i = \mathbf{e}_i \cdot \mathbf{L} \cdot \mathbf{e}_i$. Moreover, fibril bundles also rotate so that their current mean orientation directors
 114 become $\mathbf{e}_i = \mathbf{F} \cdot \mathbf{E}_i/\|\mathbf{F} \cdot \mathbf{E}_i\|$ in the deformed configuration, thus introducing a strain-induced change in

115 the structural anisotropy. Lastly, the rotation and the deformation of fibril bundles is not free and hindered
 116 by steric effects between bundles. Steric effects are captured by restraining the motion of the node C_0 with
 117 respect to its unconnected neighbors C_q . These restrictions occur along $\mathbf{e}_q = \mathbf{F} \cdot \mathbf{E}_q / \|\mathbf{F} \cdot \mathbf{E}_q\|$ at a strain
 118 rate $\dot{\varepsilon}_q = \mathbf{e}_q \cdot \mathbf{L} \cdot \mathbf{e}_q$ (see dotted lines in Fig. 1b), once the distance δ_q between C_0 and the neighboring
 119 nodes C_q exceeds a critical distance δ_c , i.e., below a contact strain $\varepsilon_q = \ln(\delta_q / \delta_c)$.
 120

121 *Mechanics of the matrix* – Regardless of the considered tissue, the mechanics of their matrix, is modeled
 122 as an incompressible hyperelastic neo-Hookean medium with a strain energy function $W = 0.5\mu(1 -$
 123 $\Phi)(\text{tr}(\mathbf{F} \cdot \mathbf{F}^T) - 3)$ which involves the shear modulus μ of the matrix.
 124

125 *Mechanics of the fibrils* – The stretch (or the compression) of each fibril of a bundle i generates a non-linear
 126 fibril reaction force. This force is noted $\mathbf{t}_i = t_i \mathbf{e}_i$ for the collagen fibrils of the *lamina propria*, and
 127 $\mathbf{t}_{im} = t_{im} \mathbf{e}_i$ and $\mathbf{t}_{ic} = t_{ic} \mathbf{e}_i$ for the collagen fibrils and the myofibrils of the *vocalis*, respectively. In order
 128 to mimic both the non-linear elasticity observed during the tension-compression of collagen fibrils as well
 129 as their time-dependent response, the following decomposition of the reaction force is proposed for the
 130 *lamina propria* (similar decompositions are proposed for t_{im} and t_{ic} in the case of the *vocalis*):

$$t_i = t_i^e + t_i^{ve}, \quad (1)$$

131 where t_i^e represents the (non-linear elastic) “neutral” response of the considered fibril, i.e., when the system
 132 attains its “relaxed” configuration. The expression proposed in Terzolo et al. (2022) is used: it provides
 133 relevant estimate of the unfolding of fibrils while accounting for their dimension (diameter d_0 , chord length
 134 ℓ_0 and tortuosity ξ_0) and mechanical properties (elastic modulus E_f). Thus, t_i^e is an hyperelastic function
 135 of ε_i :

$$t_i^e = \frac{\pi d_0^2}{4} \left[E_{eq0} \varepsilon_i + \frac{E_f - E_{eq0}}{2} \left(\varepsilon_i + \sqrt{(\varepsilon_i - \ln \xi_0)^2 + \alpha^2} - \sqrt{\ln^2 \xi_0 + \alpha^2} \right) \right], \quad (2)$$

136 when the fibril is stretched; only the first term of the bracket being kept when the fibril is compressed.
 137 This expression involves a curvature parameter α that ensures, during fibril unfolding, a proper transition
 138 between bending- and stretching-dominated regimes. In addition, the initial apparent modulus of the
 139 fibril in the folded configuration $E_{eq0} = E_f \langle \cos \beta_0 \rangle / [\langle \cos^2 \beta_0 \rangle + 16 \langle v^2 \rangle / d_0^2]$ (with $\langle \cdot \rangle = \frac{1}{\ell_0} \int_0^{\ell_0} \cdot du$,
 140 $\langle v^2 \rangle = R_0^2 / 2$ and $\beta_0 = \arctan(2\pi \frac{R_0}{H_0} \cos \frac{2\pi}{H_0} u)$) is estimated from the literature (Potier-Ferry and Siad,
 141 1992).

142 Also in Eq. (1), t_i^{ve} represents time-dependent phenomena, including those related to the fibril deformation
 143 itself, the fibril interactions with the other fibrils and/or the surrounding gel-like matrix. These molecular-
 144 scale mechanisms exhibit characteristic relaxation times (Gautieri et al., 2012; Miri et al., 2013) that
 145 are not captured by the hyperelastic formulation proposed for t_i^e in Eq. (2). A fine quantification of
 146 these transient complex processes would require molecular-scale analyses based on statistical physics or
 147 numerical simulation using molecular dynamics approaches (Gautieri et al., 2011; Bantawa et al., 2022).
 148 Here, as a first approximation, we consider a simple approach at the scale of the fibrils to account for them.
 149 Indeed, we assume that the aforementioned time-dependent phenomena can be reproduced by a non-linear
 150 viscoelastic Maxwell model, as schematized in Fig. 1a:

$$\dot{t}_i^{ve} + \frac{E}{\eta} t_i^{ve} = \pi E \frac{d_0^2}{4} \dot{\varepsilon}_i, \quad (3)$$

151 where E and η are the elastic modulus and the viscosity of the Maxwell model, respectively. As vocal-fold
 152 tissues exhibit several relaxation times over a wide range of strain rates (Chan and Titze, 1999, 2000; Chan
 153 and Rodriguez, 2008; Chan, 2018), it is necessary to include these effects in the last equation. For example,
 154 SAOS studies (Chan and Rodriguez, 2008) performed on *lamina propria* samples report a Carreau-like
 155 evolution of the complex viscosity with the shear rate, *i.e.*, with a Newtonian plateau at low shear rates
 156 and shear-thinning evolution at high shear rates. These aspects are taken into account by assuming that the
 157 viscosity η is a nonlinear Carreau function of the viscous strain rate:

$$\eta = \eta_0 \left(1 + \left(\frac{\dot{\varepsilon}_i - \frac{4\dot{t}_i^{ve}}{\pi E d_0^2}}{\dot{\varepsilon}_0} \right)^2 \right)^{\frac{n-1}{2}}, \quad (4)$$

158 where η_0 is the viscosity of the Newtonian regime, $\dot{\varepsilon}_0$ is the strain-rate transition between the Newtonian
 159 regime and the shear-thinning one, and n is the power-law index driving thinning effects at high strain rates.
 160 Expressions similar to Eqs. (2-4) are proposed for the *vocalis*, further assuming that $E_{0c} = E_{0m} = E$,
 161 $\eta_{0c} = \eta_{0m} = \eta_0$, $\dot{\varepsilon}_{c0} = \dot{\varepsilon}_{m0} = \dot{\varepsilon}_0$, $n_c = n_m = n$.

162
 163 *Steric interactions between fibril bundle* - For both tissues, once the distance δ_q between the node C_0
 164 and the neighboring nodes C_q exceeds a critical distance δ_c , *i.e.*, below a contact strain $\varepsilon_q = \ln(\delta_q/\delta_c)$,
 165 steric interactions occur via reaction forces $\mathbf{R}_q = R_q \mathbf{e}_q$. A decomposition similar to Eq. (1) is proposed to
 166 account for non-linear viscohyperelastic effects:

$$R_q = R_q^e + R_q^{ve}, \quad (5)$$

167 where the hyperelastic term R_q^e is that proposed in Terzolo et al. (2022):

$$R_q^e = \beta H(\varepsilon_q) \varepsilon_q^\kappa, \quad (6)$$

168 where H is the Heaviside function, and where β and κ are interaction parameters. To account for non-linear
 169 viscoelastic interactions, R_q^{ve} is derived from the following non-linear Maxwell equation:

$$\dot{R}_q^{ve} + \frac{E'}{\eta'} R_q^{ve} = E' s_0 \dot{\varepsilon}_q. \quad (7)$$

170 In analogy with Eq. 4, the viscosity η' is assumed to be a Carreau function of the corresponding steric
 171 strain rate:

$$\eta' = \eta'_0 \left(1 + \left(\frac{\dot{\varepsilon}_q - \frac{4\dot{R}_q^{ve}}{\pi E' d_0^2}}{\dot{\varepsilon}'_0} \right)^2 \right)^{\frac{n-1}{2}}, \quad (8)$$

172 where η'_0 is the viscosity of the Newtonian regime, and $\dot{\varepsilon}'_0$ is the transition strain-rate between the Newtonian
 173 and the thinning regime.

174 2.3 Upscaling formulation: from micro to macroscale mechanics

175 Given the structural and micromechanical features mentioned above, regardless of the tissue concerned,
 176 the macroscopic Cauchy stress tensor σ can be written as:

$$\sigma = -p\delta + \sigma_m + \sigma_f + \sigma_s \quad (9)$$

177 where p is the incompressibility pressure, δ the identity tensor, $\sigma_m = \mathbf{F} \cdot (\partial W / \partial \mathbf{F})^T$ the stress contribution
 178 of the matrix, and where σ_f and σ_s represent the stress contributions due to the (un)folding of fibrils and
 179 their steric interactions, respectively. Thus, one gets:

$$\sigma_f = \frac{\Phi}{\pi d_0^2 \xi_0} \sum_{i=1}^4 t_i \lambda_i \mathbf{e}_i \otimes \mathbf{e}_i, \quad (10)$$

180 and

$$\sigma_s = \frac{\Phi}{\pi d_0^2 \xi_0} \sum_{q=1}^5 R_q \delta_q^* \mathbf{e}_q \otimes \mathbf{e}_q \quad (11)$$

181 for the *lamina propria*, where $\delta_q^* = \delta_q / \ell_0$, and:

$$\sigma_f = \frac{\Phi_c}{\pi d_{0c}^2 \xi_{0c}} \sum_{i=1}^4 t_{ic} \lambda_i \mathbf{e}_i \otimes \mathbf{e}_i + \frac{\Phi_m}{\pi d_{0m}^2 \xi_{0m}} \sum_{i=1}^4 t_{im} \lambda_i \mathbf{e}_i \otimes \mathbf{e}_i \quad (12)$$

182 and

$$\sigma_s = \left(\frac{\Phi_c}{\pi d_{0c}^2 \xi_{0c}} + \frac{\Phi_m}{\pi d_{0m}^2 \xi_{0m}} \right) \sum_{q=1}^5 R_q \delta_q^* \mathbf{e}_q \otimes \mathbf{e}_q \quad (13)$$

183 for the *vocalis*. Thus, as an oversimplified representation, the proposed micro-mechanical model can be
 184 thought as the imbrication of two anisotropic networks of non-linear Zener models embedded in a isotropic
 185 hyperelastic matrix (Fig. 1): one for the mechanics of fibril bundles, one for their steric interactions.
 186 The mechanical response of the *lamina propria* (resp. *vocalis*) depends on 19 (resp. 25) histological and
 187 micro-mechanical parameters to be determined:

- 188 • 6 (resp. 10) *histological parameters*: the fibrils diameter d_0 (resp. d_{0c} and d_{0m}), their waviness amplitude
 189 R_0 (resp. R_{0c} and R_{0m}), spatial periodicity H_0 (resp. H_{0c} and H_{0m}) from which their tortuosity ξ_0 (resp.
 190 ξ_{0c} and ξ_{0m}) can be estimated, the fibrils volume fraction Φ (resp. Φ_c and Φ_m) and initial 3D orientation
 191 (θ_0, φ_0). These structural parameters can be determined from histological data.
- 192 • 13 (resp. 15) *mechanical parameters*: the fibrils Young's modulus modulus E_f (resp. E_{fc} and E_{fm}), the
 193 matrix shear modulus μ , the transition parameter α (resp. α_c and α_m), the elastic interaction coefficients
 194 β, κ and δ_c related to steric effects, and the viscoelastic parameters $E, \eta_0, \dot{\varepsilon}_0, n$ and $E', \eta'_0, \dot{\varepsilon}'_0$.

3 MODEL IDENTIFICATION

195 3.1 Experimental database

196 The relevance of the model was evaluated by comparing its prediction with experimental data from the
 197 literature:

- Firstly, to assess the model relevance in the linear viscoelastic regime at small shear strains, we considered the data collected by Chan and Rodriguez (2008): “cover” specimens were excised from 7 donors (2 females, 5 males), between 53 and 88 years old (mean age 67). Tissues were collected between 3 to 20 h *post-mortem* before being tested (mean time 10 h). The excised tissues were then subjected to SAOS at physiological conditions ($T \approx 37^\circ\text{C}$, 100% relative humidity). An oscillatory shear strain $\gamma_{zx} = \gamma_0 \sin(2\pi ft)$ was applied in the “longitudinal” plane ($\mathbf{e}_z, \mathbf{e}_x$), with a prescribed small shear strain amplitude $\gamma_0 = 0.01$, and a frequency f varied from 1 to 250 Hz. In the following, trends derived from these 7 donor-specific covers are represented by an “average target vocal-fold cover” noted C_{SAOS} .
- Secondly, the model ability to reproduce oscillatory responses in the non-linear regime (upon finite strains) was investigated with respect to the data reported by Chan (2018). The author subjected a 60-year-old male “cover” to LAOS with several increasing strain amplitudes $\gamma_0 = [0.05, 0.1, 0.2, 0.5, 1]$ along the plane ($\mathbf{e}_z, \mathbf{e}_x$) at a prescribed frequency $f = 75$ Hz. In the following, the sample chosen as a reference here is noted C_{LAOS} .
- Thirdly, the model prediction was compared with vocal-fold layer samples deformed at finite strains and multiaxial physiological loadings (*i.e.*, tension, compression, shear) as reported in Cochereau et al. (2020): two samples of *lamina propria* (covered by the very thin *epithelium* left intact, noted LP₁ and LP₂), and two samples of *vocalis* (noted V₁ and V₂). As a reminder, each sample was sequentially subjected to longitudinal tension along \mathbf{e}_z , transverse compression along \mathbf{e}_x , and longitudinal shear in the plane ($\mathbf{e}_z, \mathbf{e}_x$). For each loading mode, samples were subjected to 10 load/unload cycles up to Hencky strains $\varepsilon_{zz}^{max} = 0.1$, $\varepsilon_{xx}^{min} = -0.2$ and shear $\gamma_{zx}^{max} = 0.6$, at constant strain rates $|\dot{\varepsilon}_{zz}|$, $|\dot{\varepsilon}_{xx}|$ and $|\dot{\gamma}_{zx}|$ of $\approx 10^{-3} \text{ s}^{-1}$.

3.2 Optimization procedure

A protocol similar to that adopted in Terzolo et al. (2022) was applied to obtain optimized sets of histo-mechanical parameters:

- For SAOS and LAOS experiments, all histological parameters were initialized and constrained within a corridor of admissible values deduced from the literature, as detailed in Terzolo et al. (2022): $0^\circ \leq \theta_0 \leq 50^\circ$, $20^\circ \leq \varphi_0 \leq 90^\circ$, $10 \mu\text{m} \leq H_0 \leq 70 \mu\text{m}$, $1 \mu\text{m} \leq R_0 \leq 10 \mu\text{m}$, $10 \text{ nm} \leq d_0 \leq 500 \text{ nm}$, $0.15 \leq \Phi \leq 0.55$. For multi-axial experiments achieved with *lamina propria* and *vocalis* samples (Cochereau et al., 2020), we chose the histological parameters already determined in Terzolo et al. (2022), as reported in table 1.
- For SAOS and LAOS experiments, some of the hyperelastic parameters were constrained within physiological boundaries, *i.e.*, the fibril’s Young modulus $1 \text{ MPa} \leq E_f \leq 1 \text{ GPa}$, the matrix shear modulus $1 \text{ Pa} \leq \mu \leq 1.5 \text{ MPa}$. The other parameters, *i.e.*, the transition parameters α and the interaction coefficients β , κ and δ_c , were let free. It is also important to note that steric interactions are not triggered during simple shear, thus yielding to undetermined parameters β , κ , δ_c for SAOS and LAOS. For the multiaxial experiments performed with *lamina propria* and *vocalis* samples, we took the hyperelastic parameters determined in Terzolo et al. (2022), except the shear moduli of the matrices μ which were looked for in between 1 Pa and 1 MPa (see comments in the next section).
- The positive viscoelastic parameters, *i.e.*, E , η_0 , $\dot{\varepsilon}_0$, n and E' , η'_0 and $\dot{\varepsilon}'_0$ were freely optimized for each of the experiments considered. For SAOS experiments, the power-law exponent n was looked for in between 0 and 1 to mimic the recorded shear-thinning behavior (Chan and Rodriguez, 2008). As the LAOS and the multiaxial experiments were performed at a unique strain rate, n could not be determined and was arbitrarily set to the value found for SAOS experiments.

241 A non-linear constraint optimization process based on a least-squared approach was used to minimize
 242 the discrepancies between the model prediction and the experimental macroscale stress-strain curves, as
 243 in Bailly et al. (2012); Terzolo et al. (2022). The time-integration of the implicit non-linear Maxwell
 244 differential Eqs. 3 and 7 was achieved using the *ode15i* solver in Matlab[®] (Shampine, 2002).

4 RESULTS AND DISCUSSION

245 4.1 Relevance of histo-mechanical parameters

246 The set of optimized histological parameters used to reproduce the macroscopic rheological data during
 247 SAOS (Chan and Rodriguez, 2008), LAOS (Chan, 2018) and multi-axial loadings (Cochereau et al., 2020)
 248 are reported in table 1. Apart from the remarks already stated in Terzolo et al. (2022) for the relevance of
 249 these parameters for LP_i and V_i samples, these values conjure up the following comments:

Sample	θ_0 (°)	φ_0 (°)	H_0 (μm)	R_0 (μm)	d_0 (μm)	Φ	ξ_0
C _{SAOS}	10.5	83.7	34.5	7.3	0.21	0.30	1.34
C _{LAOS}	32.6	65.7	45	4.5	0.23	0.30	1.11
LP ₁	16	83	42	5	0.4	0.46	1.13
LP ₂	16	83	42.5	5	0.4	0.48	1.13
V _{1c}	33	70	28	6.4	0.4	0.1	1.4
V _{1m}	33	70	1350	130	1	0.7	1.08
V _{2c}	28	67	30	5.5	0.4	0.12	1.28
V _{2m}	28	67	1620	90	1	0.7	1.03

Table 1. Optimized histological parameters for samples C_{SAOS}, C_{LAOS}, LP₁, LP₂, V₁ and V₂. Gray-colored columns refer to quantities computed as a function of the determined histological parameters.

- 250 • The optimization led to a collagen content Φ of ≈ 0.47 for LP_i samples (*i.e.*, including the *epithelium*,
 251 the cover, the intermediate and the deep layers) *versus* only ≈ 0.30 for the cover C_{SAOS}. This finding
 252 is consistent with prior experimental evidence, showing that the first sublayer beneath the *epithelium*,
 253 *i.e.*, the superficial layer of the *lamina propria* also called "Reinke's space", exhibits a fibril content lower
 254 than that found in the intermediate and deep layers of the *lamina propria* (Hahn et al., 2006b; Walimbe
 255 et al., 2017; Bailly et al., 2018).
 256 • The optimization also yielded to a collagen fibril diameter d_0 close to 200 nm in the cover C_{SAOS},
 257 against $d_0 \approx 400$ nm in the LP_i samples. Such a decrease may be explained by the d_0 -variations reported
 258 with the collagen type (Asgari et al., 2017), and with their location across the *lamina propria* (Gray et al.,
 259 2000; Tateya et al., 2006; Hahn et al., 2006a; Muñoz-Pinto et al., 2009; Walimbe et al., 2017; Benboujja
 260 and Hartnick, 2021). In particular, Muñoz-Pinto et al. (2009) measured that the content of "thin" (resp.
 261 "thick") collagen fibrils decreases (resp. increases) steadily and about 10-fold (resp. 15-fold) from the
 262 superficial to the deep layers.
 263 • The optimized fibril tortuosity ξ_0 at rest is $\approx 20\%$ higher for the C_{SAOS} experiments than that estimated
 264 for the LP_i samples. This is consistent with previous observations showing that the intermediate layer of
 265 the *lamina propria* is characterized by a dense network of straighter ECM fibrils compared with that of
 266 the superficial and deep layers (Klepacek et al., 2016; Bailly et al., 2018).
 267 • The histological parameters found for the cover sample C_{LAOS} are very close to the values obtained
 268 for the cover samples C_{SAOS}. The main differences concern the initial fibril orientation (θ_0 and φ_0) and
 269 tortuosity (ξ_0). This can be attributed to inter-subject variability.

- 270 • The histological parameters of collagen fibrils in the *vocalis* are rather similar than those found for
 271 SAOS, LAOS and LP_i samples, except for the fibril content which is much lower. Conversely, the
 272 histological parameters of myofibrils are obviously very different.

273 In addition, the optimized micro-mechanical parameters used to reproduce the macroscopic rheological
 274 data during SAOS (Chan and Rodriguez, 2008), LAOS (Chan, 2018) and multi-axial loadings (Cochereau
 275 et al., 2020) are reported in tables 2 and 3 for hyperelastic and viscoelastic contributions, respectively. The
 276 reader is referred to Terzolo et al. (2022) for the relevance of the hyperelastic parameters in the cases of the
 277 LP_i and V_i samples. Also, the following remarks can be brought:

Sample	E_f (MPa)	μ (Pa)	α	β (N)	κ	δ_c (μm)
C _{SAOS}	720	31	$1.6 \cdot 10^{-3}$	-	-	-
C _{LAOS}	720	30	$4.6 \cdot 10^{-3}$	-	-	-
LP ₁	847	200	$4.4 \cdot 10^{-3}$	$2 \cdot 10^{-4}$	3	66
LP ₂	847	190	$4.3 \cdot 10^{-3}$	$4 \cdot 10^{-4}$	3	65.7
V _{1c}	847	170	$4.4 \cdot 10^{-3}$	$2.2 \cdot 10^{-4}$	3	367
V _{1m}	0.05	170	$1.1 \cdot 10^{-2}$	$2 \cdot 10^{-4}$	3	367
V _{2c}	847	170	$4.4 \cdot 10^{-3}$	$7.6 \cdot 10^{-5}$	3	360
V _{2m}	0.05	170	$2.7 \cdot 10^{-2}$	$7.6 \cdot 10^{-5}$	3	360

Table 2. Optimized hyperelastic parameters for samples C_{SAOS}, C_{LAOS}, LP₁, LP₂, V₁ and V₂.

Sample	E (MPa)	η_0 (MPa s)	$\dot{\varepsilon}_0$ (s^{-1})	n	E' (MPa)	η'_0 (MPa s)	$\dot{\varepsilon}'_0$ (s^{-1})
C _{SAOS}	3.68	1.56	2.1×10^{-3}	0.27	-	-	-
C _{LAOS}	4.19	1.14	1.9×10^{-3}	0.27	-	-	-
LP ₁	1.47	14.2	5×10^{-4}	0.27	0.99	8.3	5.5×10^{-3}
LP ₂	1.3	19.6	6×10^{-4}	0.27	1.63	16	4.5×10^{-3}
V ₁	0.11	0.38	3.6×10^{-3}	0.27	0.11	0.53	4.5×10^{-3}
V ₂	0.11	1.06	3.3×10^{-3}	0.27	0.07	0.67	4.5×10^{-3}

Table 3. Optimized viscoelastic parameters for samples C_{SAOS}, C_{LAOS}, LP₁, LP₂, V₁ and V₂.

- 278 • For the LP_i and V_i samples, the shear modulus of the matrix μ -coefficient was re-optimized
 279 (within physiological boundaries) as the mechanical contribution of the matrix is here related both
 280 to the hyperelastic and the viscoelastic contributions (which encompass the fibrils/surrounding matrix
 281 interactions). Thus, the optimization process led to (200 Pa, 190 Pa) for (LP₁, LP₂), against (330 Pa,
 282 290 Pa) in Terzolo et al. (2022); and to 170 Pa for both V_i samples, against (900 Pa, 980 Pa).
- 283 • As emphasized in table 2, the matrix shear modulus μ is nearly 10-fold lower for the cover samples
 284 C_{SAOS} and C_{LAOS} than for the entire LP_i samples. The value identified for C_{SAOS} and C_{LAOS} are close
 285 to the range measured for the elastic shear modulus of hyaluronic acid $\mu_{HA} \approx 20\text{--}50$ Pa (estimated at
 286 loading frequencies up to 10 Hz; Heris et al. (2012)), *i.e.*, the most abundant polymer of the ground
 287 substance in the *lamina propria*. Known to play a key role in shock absorption during vocal-fold collisions,
 288 hyaluronic acid is found with a higher volume fraction than collagen and elastin in the superficial layer,
 289 by contrast with the deep layer (Finck, 2008; Hahn et al., 2006a,b), which is in line with the identification
 290 result (see table 1). The observed discrepancy in μ -values in table 2 is probably ascribed to the scarcity

291 of elastin fibrils reported in the superficial layer (and therefore in the cover) in elderly tissues (Roberts
292 et al., 2011).

- 293 • The hyperelastic parameters related to the collagen fibril networks are very similar regardless of the
294 considered samples, *i.e.*, SAOS, LAOS and LP_i and V_i samples. Due to the much softer passive mechanics
295 of myofibrils, their hyperelastic parameters are much lower. Probably for the same reason, the optimized
296 viscoelastic parameters (E , η_0 , $\dot{\varepsilon}_0$) found for the *lamina propria*, the SAOS and for the LAOS samples
297 differ by an order of magnitude with those reported for the *vocalis*.
- 298 • The viscoelastic parameters of the LP_i samples have been identified at a very low strain rate, *i.e.*, close
299 to $\dot{\varepsilon}_0$. At this strain rate, the relaxation times $\tau \approx \eta_0/E \approx 3\text{--}15$ s are obtained for both vocal-fold layers
300 (similar relaxation times $\tau' = \eta'_0/E'$ were found for fibril bundle steric hindrance). It is interesting to
301 note that these results are in line with the rare experimental data available at this scale (Yang, 2008;
302 Shen et al., 2011; Gautieri et al., 2011). For example Shen et al. (2011) report typical relaxation times
303 of solvated collagen fibrils in the range of 7–102 s. Also, Yang (2008) measured two distinct processes
304 contributing to the stress relaxation of native collagen fibrils immersed in PBS buffer and subjected to
305 5–7 % strain for 5–10 min: a fast relaxation process with a characteristic time $\tau_1 \approx 1.8 \pm 0.4$ s, and a
306 slow relaxation process with $\tau_2 \approx 60 \pm 10$ s. Yang proposed that τ_1 corresponds to the relative sliding
307 of collagen microfibrils, while τ_2 refers to the relative sliding of collagen molecules (due to the high
308 level of cross-links between molecules). It is interesting to note that the characteristic times reported
309 for the SAOS and LAOS samples are markedly lower, *i.e.*, $\tau = \eta_0/E \approx 0.42$ s and 0.27 s, respectively.
310 Bearing in mind that the model parameters for SAOS and LAOS were determined from experimental
311 data acquired at high frequencies (from 1 to 250 Hz for SAOS, and at 75 Hz for LAOS), these low valued
312 characteristic times are not surprising: additional data at lower strain rates would probably increase these
313 values.

314 4.2 Relevance of the micro-mechanical model for SAOS

315 A comparison between the model predictions at macroscale and the SAOS experimental data is provided in
316 Fig. 2. In this figure, graphs (a) and (b) show the evolution of the shear storage and loss moduli G' and
317 G'' of sample C_{SAOS} as functions of the excitation frequency f , whereas graphs (c) and (d) do the same
318 for the loss factor $\zeta^* = G''/G'$ and the dynamic viscosity $\mu' = G''/2\pi f$, respectively. In these graphs, the
319 model predictions were extended up to $f = 1$ kHz. Different remarks are highlighted from these graphs:

- 320 • For all the rheological functions presented, a fairly good quantitative agreement is obtained between the
321 model predictions (continuous lines) and the experimental data (marks): progressive increase of storage
322 and loss moduli G' and G'' with f up to 200 Hz, power-law decrease of the viscosity μ' , Carreau-like
323 evolution of the loss factor ζ^* with a mark power-law decrease above 10–50Hz.
- 324 • More particularly, it is interesting to note that the model nicely predicts the experimental “cross-over”
325 zone around 50–100 Hz, *i.e.*, the zone within which (i) the storage modulus G' switches from lower to
326 higher than the loss modulus G'' , (ii) the loss factor ζ^* switches from constant to remarkable decrease.
327 This transition zone also coincides with that where some issues occur during vocal-fold vibration in
328 human phonation. In fact, for fold vibration at low frequencies, *i.e.*, below 50–100 Hz, viscous effects
329 dominate ($G'' \geq G'$) so that this should give rise to critical tissue overdamping preventing proper periodic
330 oscillations of vocal folds. In contrast, the dominant elastic properties at higher frequencies should
331 restrain tissue damping (see the power-law decrease of the loss factor in Fig. 2(c)), thus allowing the
332 occurrence of proper periodic motion during vocal fold vibration (Chan and Rodriguez, 2008).

333 • To illustrate the role of histological parameters on the rheological response of SAOS samples, we have
334 reported two additional discontinuous lines in Fig. 2. These trends emphasize the effects induced by
335 variations of the volume fraction of collagen fibrils Φ (here, Φ was chosen due to its wide variations
336 between individuals but also within the vocal-fold layers themselves): the case where $\Phi = 0.15$ and
337 the case where $\Phi = 0.55$, *i.e.*, the minimum and maximum values found in the literature for *lamina*
338 *propria*. As shown in Fig. 2, when Φ varies in the physiological corridor, the qualitative trends are
339 preserved for all viscoelastic properties (G' , G'' , ζ^* and μ'). However, the higher the fibril content, the
340 higher the rheological functions, albeit with (i) marked differences (for G' at high frequencies, for ζ^*
341 at low frequencies, *e.g.*, for G'' , μ' at all frequencies) and with (ii) a slight shift of the cross-over zone
342 towards lower frequencies as Φ is increased. Note that the case of $\Phi \approx 0$ was also predicted in Fig. 2 as
343 a theoretical extreme case (not physiological), assuming a quasi-total absence of collagen fibers in the
344 vocal-fold cover, which would thus become close to a homogeneous, isotropic neo-hookean material
345 with the same mechanical properties as the matrix alone. These simulations clearly emphasize the major
346 mechanical role played by the collagen fibrous network, and its interaction with the surrounding ground
347 substance, in response to the oscillatory shear of the vocal-fold cover.
348

349 4.3 Relevance of the micro-mechanical model for LAOS

350 In Fig. 3a, we have reported a collection of Lissajous stress-strain curves predicted by the model. These
351 curves are compared with LAOS experiments obtained at a frequency $f = 75$ Hz and cyclic amplitudes
352 γ_0 varied from 0.05 to 0.5. In addition, Fig. 3b presents a series of normalized Lissajous stress-strain
353 curves predicted by the model in the Pipkin space $\{f, \gamma_0\}$ or $\{f, \varepsilon_i^{max}\}$ (ε_i^{max} is the maximal cyclic tensile
354 strain the fibrils are subjected to), when f and γ_0 are varied from 50 Hz to 1kHz and from 0.05 to 0.5,
355 respectively (Ewoldt et al., 2008; Chan, 2018). Within each contour plot, the black line represents the total
356 visco-hyperelastic stress, whereas the red line is the hyperelastic or neutral stress contribution. Different
357 trends can be highlighted:

358 • *Influence of the strain amplitude γ_0* – Fig. 3a shows a very good quantitative agreement between the
359 model predictions (red line) and the experimental data at stabilized cycles when $\gamma_0 \leq 0.2$. In particular,
360 the model is able to capture the strong non-linear response of the tested sample with, in particular, a proper
361 modeling of the stress hysteresis induced by viscoelastic effects. In addition, the cyclic stress-strain curves
362 progressively deviate from a linear strain hardening at low shear strain amplitudes ($\gamma_0 \leq 0.1$), which
363 corresponds to the initial linear (un)folding of collagen fibril at small strains, towards a marked non-linear
364 strain-hardening at higher strain magnitudes (in J-shape), where the non-linear hyperelastic stretching of
365 collagen fibrils is triggered. This trend is also fairly well illustrated by the neutral stress responses of the
366 Pipkin diagram shown in Fig. 3b. This diagram also proves that the trend is preserved independently of
367 the cycling frequency. Lastly, it is worth noticing from Fig. 3a that the predicted strain-hardening at the
368 highest strain magnitude $\gamma_0 = 0.5$ largely overestimates the cycle observed experimentally. Presumably,
369 during the experiments, the tested cover exhibited a Mullins-like effect, as often observed in elastomers,
370 gels and soft living tissues (Diani et al., 2009; Peña et al., 2009; Rebouah et al., 2017; Rebouah and
371 Chagnon, 2014; Zhan et al., 2024). This could yield to a stress softening of their mechanical behavior
372 upon cycling. The Mullins effect can be caused by a number of irreversible mechanisms, *e.g.*, the rupture
373 of physical or covalent cross-links and the possible disentanglement of molecular chains, *etc.* These
374 mechanisms are not taken into account in the current micro-mechanical model. Yet, a possible way
375 to account for these phenomena would consist in altering, with proper kinetics, the histo-mechanical

376 properties of the collagen fibrils, such as their modulus E_f (to account for damage) and/or their initial
 377 length ℓ_0^f or tortuosity ξ_0 (to account for disentanglement). In support of this hypothesis to be explored in
 378 future work, Fig. 3a shows that lowering (resp. increasing) E_f (resp. ξ_0) from 720 MPa to 400 MPa (resp.
 379 from 1.11 to 1.12) would lead to a more appropriate model prediction of the experimental stress-strain
 380 curve performed at $\gamma_0 = 0.5$ (see green line).

381 • *Influence of the loading frequency f* – As shown in Fig. 3b, the loading frequency f markedly alters
 382 the Lissajous curves. Regardless of the strain magnitude γ_0 , the higher the f -value, the higher the stress
 383 levels and the stress hysteresis. These trends are in qualitative agreement with measurements acquired on
 384 other vocal-fold cover samples (Chan, 2018).

385 4.4 Relevance of the micro-mechanical model for finite strain multi-axial cyclic loadings

386 Macroscopic stress-strain predictions are compared with the reference experimental data in Fig. 4 (resp.
 387 Fig. 5), for the *lamina propria* and *vocalis* samples LP₁ and V₁ (resp. LP₂ and V₂), and the three cyclic
 388 loadings these samples were subjected to, *i.e.*, longitudinal tension, transverse compression and longitudinal
 389 shear. For each case, the “neutral” curve already predicted in Terzolo et al. (2022) was reported (see dotted
 390 lines). The strain-induced evolution of micro-mechanical descriptors during cyclic tension is displayed
 391 in Fig. 6 (illustrative case of LP₁ and V₁), with compression and shear results summarized in Fig. 7
 392 (illustrative case of LP₁).

393 The results for the first loading cycle are discussed below for each loading mode:

394 • *Longitudinal tension* – The model prediction for longitudinal tension along e_z is fairly good both for the
 395 *lamina propria* and the *vocalis* samples, as emphasized in Figs. 4- 5(a). In particular, compared with the
 396 hyperelastic formulation proposed in Terzolo et al. (2022), *i.e.*, the neutral curves, the model is now able to
 397 capture the stress hysteresis as well as the residual strains after unloading. These tendencies are inherited
 398 from microscale viscoelastic effects together with the rearrangement of the tissue microstructures. This is
 399 illustrated in Fig. 6 and Supplementary Fig. S1, in which one can assess the irreversible unfolding and
 400 rotation of fibrils that are predicted during cyclic tension both for the *lamina propria* and the *vocalis*
 401 samples. It is interesting to note that the predicted stress hysteresis and residual strain of collagen fibrils
 402 were experimentally observed by Yang (2008). For the *vocalis*, the predicted tensions in both collagen
 403 fibrils, t_{ic} , and myofibrils, t_{im} , are plotted in the inset of Fig. 6b. If the key role played by the sheaths of
 404 collagen fibers surrounding muscle fibers in the tissue passive tensile properties was already evidenced
 405 during monotonic loading, the strong contribution of myofibrils to inelastic effects and residual strains
 406 after unloading is here clearly highlighted.

407 • *Transverse compression* – Figs. 4- 5(b) prove that the model predictions are also in good agreement
 408 with the experimental data recorded during transverse compression. Moreover, as already pointed out in
 409 Terzolo et al. (2022), steric interactions are of major importance for the *lamina propria* and the *vocalis*
 410 mechanics during compression. This characteristic is preserved with the visco-hyperelastic formulation:
 411 if steric hindrance effects are deactivated in the model (see model predictions with “no steric interactions”
 412 in Figs. 4- 5(b), dash-dotted lines), the deformation of the visco-hyperelastic fibril bundles is not sufficient
 413 to capture the *lamina propria* stress hysteresis and residual strain experimentally observed. Thus, fibril
 414 bundle repulsion forces R_q and their viscoelastic contributions R_q^{ve} , appear to be of critical importance
 415 to properly reproduce the compression behavior of both vocal-fold layers (see “model predictions” in
 416 Figs. 4- 5(b), solid lines). No other significant microscale deformation mechanisms (such as rotation
 417 and/or noticeable unfolding of fibrils) were predicted under transverse compression (Fig. 7a).

418 • *Longitudinal shear* – The mechanical contribution of the matrix plays a major role in the overall shear
419 response of the *lamina propria* and the *vocalis*, as already stressed in Terzolo et al. (2022). On this basis,
420 the fibrils viscoelastic properties and interactions with the surrounding ground substance allowed, *via* the
421 microscopic tension t_i (Fig. 7b), to satisfactorily reproduce the experimental trends observed during the
422 load/unload sequence at the tissue scale (Figs. 4- 5c).

423 Finally, the relevance of the visco-hyperelastic model to simulate the sequential series of 10 load-unload
424 cycles and the tissue response as a function of load history is assessed. Figure 8 compares the theoretical
425 predictions with the reference cyclic data for the three loading modes. If the decrease in stress hysteresis is
426 qualitatively well captured by the model once the first cycle has been completed in tension, compression
427 and shear, the predictions fail to simulate the progressive decrease in peak stresses measured after repeated
428 loading paths, as well as the increase in residual strains after repeated unloading paths, which are particularly
429 observed in tension and compression. According to the model, a steady state is reached practically after the
430 first load/unload sequence, whereas stabilized behavior is only really observed experimentally after the 5th
431 cycle (or even up to the 10th cycle, depending on the sample and loading mode). As mentioned for LAOS
432 results, these accommodation behaviors resemble Mullins-like effects, that are not taken into account in
433 the present formulation of the model.

434

435 4.5 Relevance of the model for predicting future patho/physiological variations and 436 assisting biomedical developments

437 The micromechanical model developed in this work has been calibrated to reproduce the microstructural
438 specificities and multiscale behavior of healthy human vocal-fold tissues, combining a wide range of
439 histomechanical measurements collected from the available literature. By adjusting these input data, it can
440 be adapted and used to predict the multiscale mechanical behavior of pathological human vocal tissues
441 (Hantzakos et al., 2009; Finck, 2008), animal vocal tissues (Li et al., 2024), or structured (bio)composites
442 developed to replace/reconstruct the fibrous architecture and vibromechanical performance of the vocal
443 folds after surgery (Heris et al., 2012; Li et al., 2016; Jiang et al., 2019; Latifi et al., 2018; Ravanbakhsh
444 et al., 2019; Ferri-Angulo et al., 2023).

445 It can also be used to predict the evolution of the mechanical properties of the same tissue following an
446 alteration in its microstructural arrangement, due, for example, to its natural growth and remodeling with
447 age (by simulating a progressive decrease in the volume fraction of elastin, an increase in that of collagen,
448 and muscle atrophy (Roberts et al., 2011; Kuhn, 2014; Li et al., 2024)); due to scarring lesions acquired
449 on the tissue (by simulating fibrosis and an increase in the collagen content as well as changes in fibrils
450 tortuosity as compared to the healthy case (Heris et al., 2015; Li et al., 2016)); due to the appearance of
451 a lesion following phonotrauma (by simulating damage mechanisms likely to occur at the fibril's level
452 (Miller and Gasser, 2022)); or due to a therapeutic treatment (simulating the addition of a soft hydrogel to
453 the matrix composite, for example (Li et al., 2016; Mora-Navarro et al., 2026)).

454 In order to better understand the impact of these histological variations on vocal-fold vibrations at the
455 larynx level (in the case of native tissue but also injured, repaired and/or replaced tissue), this original
456 constitutive law should be implemented in a finite element code reproducing the vocal folds in their
457 3D anatomical geometry, as in current 3D phonation models (Döllinger, M. et al., 2023). In doing so,
458 microstructure-based simulations could not only improve knowledge of the links between the specific
459 microarchitecture of the vocal folds and their unique macroscale vibratory performance, but also guide the

460 design and optimization of fibre-reinforced biomaterials currently under development for functional vocal
461 restoration.

5 CONCLUSION

462 A better understanding of human phonation requires an in-depth study of the viscoelastic properties of
463 vocal folds. To this end, this study proposes to enrich a recent 3D micro-mechanical model of vocal-fold
464 tissues, hitherto capable of predicting their nonlinear elastic and anisotropic mechanical behavior at various
465 spatial scales (micro to macro) (Terzolo et al., 2022). This was achieved by adding viscoelastic mechanisms
466 at the scale of their collagen fibrils and myofibrils bundles. These improvements now enable the model to
467 capture the viscoelastic properties of vocal-fold tissues from small to finite strains, such as their nonlinear
468 strain-rate sensitivity – on which their damping and oscillation onset properties strongly depend, their
469 stress hysteretic response and inelastic deformations typically measured during cyclic loading. In addition,
470 the model allows the microstructural rearrangements to be predicted, which is often very challenging to
471 identify experimentally.

472 This model was successfully used to reproduce various sets of *ex vivo* data available in the literature, and to
473 complement them with original theoretical data, providing specific micro-mechanism scenarios for each.
474 This identification was carried out for a wide variety of loading conditions at different rates: low-frequency
475 cyclic tension, compression and shear in large deformations; high-frequency oscillatory shear from small
476 to large deformations (SAOS for the linear viscoelasticity regime, LAOS for the nonlinear viscoelasticity
477 regime). The model predictions are in quantitative agreement with macroscopic experimental trends, and
478 clearly highlight the key impact of microscopic histomechanical descriptors on vocal-fold dynamics, such
479 as the volume fraction of collagen fibrils in the cover, their tortuosity at rest, their mechanics and their
480 interactions. This micromechanical model can be implemented in finite element codes to further simulate
481 the transient dynamics of vocal folds with relevant histo-mechanical properties.

482 However, some model limitations should be improved. For example, (coarsed grained) atomistic/molecular
483 simulations would probably provide relevant information to strengthen the physical links between the
484 time-dependent nanostructural rearrangements and the phenomenological approach proposed herein at
485 the fibril scale. Furthermore, the model does not allow the Mullins-like effects commonly observed in
486 vocal tissues to be adequately described: combined with additional experiments focused on this aspect, the
487 model could be improved based on formulations proposed for other materials such as structured elastomers
488 (Rebouah and Chagnon, 2014; Rebouah et al., 2017).

DATA AVAILABILITY

489 The datasets generated and/or analysed during the current study are available from the corresponding author
490 upon request.

FUNDING

491 This work was funded by the ANR MicroVoice (Grant No. ANR-17-CE19-0015-01) and the LabEx Tec21
492 (Investissements d’Avenir - Grant Agreement No. ANR-11-LABX-0030). The 3SR Lab is part of the
493 PolyNat Carnot Institute (Investissements d’Avenir - Grant Agreement No. ANR16-CARN0025-01).

ACKNOWLEDGMENTS

494 We would like to thank Nathalie Henrich Bernardoni (CNRS, Gipsa-lab, Grenoble) for her helpful assistance
495 in this work.

CONFLICT OF INTEREST

496 The authors declare that the research was conducted in the absence of any commercial or financial
497 relationships that could be construed as a potential conflict of interest.

REFERENCES

- 498 Asgari, M., Latifi, N., Heris, H. K., Vali, H., and Mongeau, L. (2017). In vitro fibrillogenesis of
499 tropocollagen type III in collagen type I affects its relative fibrillar topology and mechanics. *Scientific
500 Reports* 7, 1392–undefined. doi:10.1038/s41598-017-01476-y
- 501 Bailly, L., Cochereau, T., Orgéas, L., Henrich Bernardoni, N., Rolland du Roscoat, S., McLeer-Florin, A.,
502 et al. (2018). 3D multiscale imaging of human vocal folds using synchrotron X-ray microtomography in
503 phase retrieval mode. *Scientific Reports* 8. doi:10.1038/s41598-018-31849-w
- 504 Bailly, L., Geindreau, C., Orgéas, L., and Deplano, V. (2012). Towards a biomimetism of abdominal
505 healthy and aneurysmal arterial tissues. *Journal of the Mechanical Behavior of Biomedical Materials* 10,
506 151–165. doi:10.1016/j.jmbbm.2012.02.019
- 507 [Dataset] Bantawa, M., Keshavarz, B., Geri, M., Bouzid, M., Divoux, T., McKinley, G. H., et al. (2022).
508 The hidden hierarchical nature of soft particulate gels
- 509 Benboujja, F. and Hartnick, C. (2021). Quantitative evaluation of the human vocal fold extracellular matrix
510 using multiphoton microscopy and optical coherence tomography. *Scientific Reports* 11, 2440
- 511 Chan, R. W. (2004). Measurements of vocal fold tissue viscoelasticity: Approaching the male phonatory
512 frequency range. *The Journal of the Acoustical Society of America* 115, 3161–3170. doi:10.1121/1.
513 1736272
- 514 Chan, R. W. (2018). Nonlinear viscoelastic characterization of human vocal fold tissues under large-
515 amplitude oscillatory shear (LAOS). *Journal of Rheology* 62, 695–712. doi:10.1122/1.4996320
- 516 Chan, R. W. and Rodriguez, M. L. (2008). A simple-shear rheometer for linear viscoelastic characterization
517 of vocal fold tissues at phonatory frequencies. *The Journal of the Acoustical Society of America* 124,
518 1207–1219. doi:10.1121/1.2946715
- 519 Chan, R. W. and Titze, I. R. (1999). Viscoelastic shear properties of human vocal fold mucosa: measurement
520 methodology and empirical results. *The Journal of the Acoustical Society of America* 106, 2008–21.
521 doi:10.1121/1.427947
- 522 Chan, R. W. and Titze, I. R. (2000). Viscoelastic shear properties of human vocal fold mucosa: Theoretical
523 characterization based on constitutive modeling. *The Journal of the Acoustical Society of America* 107,
524 565–580. doi:10.1121/1.428354
- 525 Cochereau, T., Bailly, L., Orgéas, L., Henrich Bernardoni, N., Robert, Y., and Terrien, M. (2020).
526 Mechanics of human vocal folds layers during finite strains in tension, compression and shear. *Journal
527 of Biomechanics* 110. doi:10.1016/j.jbiomech.2020.109956
- 528 Dashatan, S. H., Sit, M., Zhang, Z., Grossmann, E., Millot, J., Huang, Y., et al. (2023). Enhanced vibration
529 damping and viscoelastic properties of flax/epoxy composites and their carbon fibre hybrid laminates.
530 *Composites Part A: Applied Science and Manufacturing* 175, 107819. doi:<https://doi.org/10.1016/j.compositesa.2023.107819>

- 532 DeJonckere, P. and Lebacq, J. (2020). Lung volume affects the decay of oscillations at the end of a vocal
533 emission. *Biomedical Signal Processing and Control* 62, 102148. doi:<https://doi.org/10.1016/j.bspc.2020.102148>
- 535 Diani, J., Fayolle, B., and Gilormini, P. (2009). A review on the Mullins effect. *European Polymer Journal*
536 45, 601–612. doi:[10.1016/J.EURPOLYMJ.2008.11.017](https://doi.org/10.1016/J.EURPOLYMJ.2008.11.017)
- 537 Döllinger, M., Zhang, Z., Schoder, S., Šidllof, P., Tur, B., and Kniesburges, S. (2023). Overview on
538 state-of-the-art numerical modeling of the phonation process. *Acta Acust.* 7, 25. doi:[10.1051/aacus/2023014](https://doi.org/10.1051/aacus/2023014)
- 540 Ewoldt, R. H., Hosoi, A. E., and McKinley, G. H. (2008). New measures for characterizing nonlinear
541 viscoelasticity in large amplitude oscillatory shear. *Journal of Rheology* 52, 1427–1458. doi:[10.1122/1.2970095](https://doi.org/10.1122/1.2970095)
- 543 Ferri-Angulo, D., Yousefi-Mashouf, H., Michel, M., McLeer, A., Orgéas, L., Bailly, L., et al. (2023).
544 Versatile fiber-reinforced hydrogels to mimic the microstructure and mechanics of human vocal-fold
545 upper layers. *Acta Biomaterialia* 172, 92–105. doi:<https://doi.org/10.1016/j.actbio.2023.09.035>
- 546 Finck, C. (2008). *Implantation d'acide hyaluronique estérifié lors de la microchirurgie des lésions cordales bénignes*. Ph.D. thesis, Université de Liège, Liège
- 548 Gautieri, A., Vesentini, S., Redaelli, A., and Buehler, M. J. (2011). Hierarchical structure and
549 nanomechanics of collagen microfibrils from the atomistic scale up. *Nano Letters* 11, 757–766.
550 doi:[10.1021/nl103943u](https://doi.org/10.1021/nl103943u)
- 551 Gautieri, A., Vesentini, S., Redaelli, A., and Buehler, M. J. (2012). Viscoelastic properties of model
552 segments of collagen molecules. *Matrix Biology* 31, 141–149. doi:[10.1016/j.matbio.2011.11.005](https://doi.org/10.1016/j.matbio.2011.11.005)
- 553 Gray, S. D., Alipour, F., Titze, I. R., and Hammond, T. H. (2000). Biomechanical and histologic
554 observations of vocal fold fibrous proteins. *Annals of Otology, Rhinology and Laryngology* 109, 77–85.
555 doi:[10.1177/000348940010900115](https://doi.org/10.1177/000348940010900115)
- 556 Hahn, M. S., Kobler, J. B., Starcher, B. C., Zeitels, S. M., and Langer, R. (2006a). Quantitative and
557 comparative studies of the vocal fold extracellular matrix I: elastic fibers and hyaluronic acid. *Annals of
558 Otology, Rhinology and Laryngology* 115, 156–164. doi:[10.1177/000348940611500213](https://doi.org/10.1177/000348940611500213)
- 559 Hahn, M. S., Kobler, J. B., Zeitels, S. M., and Langer, R. (2006b). Quantitative and comparative studies
560 of the vocal fold extracellular matrix II: collagen. *Annals of Otology, Rhinology and Laryngology* 115,
561 225–232. doi:[10.1177/000348940611500311](https://doi.org/10.1177/000348940611500311)
- 562 Hantzakos, A., Remacle, M., Dikkers, F. G., Degols, J. C., Delos, M., Friedrich, G., et al. (2009). Exudative
563 lesions of Reinke's space: A terminology proposal. *European Archives of Oto-Rhino-Laryngology* 266,
564 869–878. doi:[10.1007/s00405-008-0863-x](https://doi.org/10.1007/s00405-008-0863-x)
- 565 Heris, H. K., Latifi, N., Vali, H., Li, N., and Mongeau, L. (2015). Investigation of Chitosan-glycol/glyoxal
566 as an Injectable Biomaterial for Vocal Fold Tissue Engineering. *Procedia Engineering* 110, 143–150.
567 doi:[10.1016/j.proeng.2015.07.022](https://doi.org/10.1016/j.proeng.2015.07.022)
- 568 Heris, H. K., Rahmat, M., and Mongeau, L. (2012). Characterization of a Hierarchical Network of
569 Hyaluronic Acid/Gelatin Composite for use as a Smart Injectable Biomaterial. *Macromolecular
570 Bioscience* 12, 202–210. doi:[10.1002/mabi.201100335](https://doi.org/10.1002/mabi.201100335)
- 571 Hirano, M. (1974). Morphological structure of the vocal cord as a vibrator and its variations. *Folia
572 Phoniatrica et Logopaedica* 26, 89–94. doi:[10.1159/000263771](https://doi.org/10.1159/000263771)
- 573 Jiang, L., Jiang, Y., Stiadle, J., Wang, X., Wang, L., Li, Q., et al. (2019). Electrospun nanofibrous
574 thermoplastic polyurethane/poly(glycerol sebacate) hybrid scaffolds for vocal fold tissue engineering
575 applications. *Materials Science and Engineering: C* 94, 740–749. doi:<https://doi.org/10.1016/j.msec.2018.10.027>

- 577 Kelleher, J. E., Siegmund, T., Du, M., Naseri, E., and Chan, R. W. (2013a). Empirical measurements
578 of biomechanical anisotropy of the human vocal fold lamina propria. *Biomechanics and Modeling in*
579 *Mechanobiology* 12, 555–567. doi:10.1007/s10237-012-0425-4
- 580 Kelleher, J. E., Siegmund, T., Du, M., Naseri, E., and Chan, R. W. (2013b). The anisotropic hyperelastic
581 biomechanical response of the vocal ligament and implications for frequency regulation: a case study.
582 *The Journal of the Acoustical Society of America* 133, 1625–1636. doi:10.1121/1.4776204
- 583 Klemuk, S. A. and Titze, I. R. (2004). Viscoelastic properties of three vocal-fold injectable biomaterials at
584 low audio frequencies. *Laryngoscope* 114, 1597–1603. doi:10.1097/00005537-200409000-00018
- 585 Klepacek, I., Jirak, D., Duskova Smrckova, M., Janouskova, O., and Vampola, T. (2016). The Human Vocal
586 Fold Layers. Their Delineation Inside Vocal Fold as a Background to Create 3D Digital and Synthetic
587 Glottal Model. *Journal of Voice* 30, 529–537. doi:10.1016/j.jvoice.2015.08.004
- 588 Klos, A., Bailly, L., Rolland du Roscoat, S., Orgéas, L., Henrich Bernardoni, N., Broche, L., et al. (2024).
589 Optimising 4d imaging of fast-oscillating structures using x-ray microtomography with retrospective
590 gating. *Scientific Reports* 14, 20499. doi:10.1038/s41598-024-68684-1
- 591 Koruk, H. and Rajagopal, S. (2024). A comprehensive review on the viscoelastic parameters used
592 for engineering materials, including soft materials, and the relationships between different damping
593 parameters. *Sensors* 24. doi:10.3390/s24186137
- 594 Kuhn, M. (2014). Histological changes in vocal fold growth and aging. *Current Opinion in Otolaryngology*
595 & Head and Neck Surgery
- 596 Latifi, N., Asgari, M., Vali, H., and Mongeau, L. (2018). A tissue-mimetic nano-fibrillar hybrid injectable
597 hydrogel for potential soft tissue engineering applications. *Scientific Reports*, 1047doi:10.1038/
598 s41598-017-18523-3
- 599 Li, L., Stiadle, J. M., Lau, H. K., Zerdoum, A. B., Jia, X., Thibeault, S. L., et al. (2016). Tissue
600 engineering-based therapeutic strategies for vocal fold repair and regeneration. *Biomaterials* 108,
601 91–110. doi:10.1016/j.biomaterials.2016.08.054
- 602 Li, X., Lin, X., Xie, X., Chen, X., Xie, Y., and Sun, G. (2024). Histological characterization of rat
603 vocal fold across different postnatal periods. *Laryngoscope Investigative Otolaryngology* 9, e70018.
604 doi:<https://doi.org/10.1002/liv2.70018>
- 605 Miller, C. and Gasser, T. C. (2022). A bottom-up approach to model collagen fiber damage and failure
606 in soft biological tissues. *Journal of the Mechanics and Physics of Solids* 169, 105086. doi:<https://doi.org/10.1016/j.jmps.2022.105086>
- 608 Miri, A. K. (2014). Mechanical characterization of vocal fold tissue: a review study. *Journal of Voice* 28,
609 657–667. doi:10.1016/j.jvoice.2014.03.001
- 610 Miri, A. K., Heris, H. K., Mongeau, L., and Javid, F. (2014). Nanoscale viscoelasticity of extracellular
611 matrix proteins in soft tissues: a multiscale approach. *Journal of the Mechanical Behavior of Biomedical*
612 *Materials* 30, 196–204. doi:10.1016/j.jmbbm.2013.10.022
- 613 Miri, A. K., Heris, H. K., Tripathy, U., Wiseman, P. W., and Mongeau, L. (2013). Microstructural
614 characterization of vocal folds toward a strain-energy model of collagen remodeling. *Acta Biomaterialia*
615 9, 7957–7967. doi:10.1016/j.actbio.2013.04.044
- 616 Mora-Navarro, C., Smith, E., Wang, Z., del C. Ramos-Alamo, M., Collins, L., Awad, N., et al. (2026).
617 Injection of vocal fold lamina propria-derived hydrogels modulates fibrosis in injured vocal folds.
618 *Biomaterials Advances* 178, 214424. doi:<https://doi.org/10.1016/j.bioadv.2025.214424>
- 619 Muñoz-Pinto, D., Whittaker, P., and Hahn, M. S. (2009). Lamina propria cellularity and collagen
620 composition: an integrated assessment of structure in humans. *The Annals of Otology, Rhinology and*
621 *Laryngology* 118, 299–306. doi:10.1177/000348940911800411

- 622 Peña, E., Peña, J. A., and Doblaré, M. (2009). On the Mullins effect and hysteresis of fibered biological
623 materials: A comparison between continuous and discontinuous damage models. *International Journal*
624 *of Solids and Structures* 46, 1727–1735. doi:10.1016/j.ijsolstr.2008.12.015
- 625 Potier-Ferry, M. and Siad, L. (1992). Homogénéisation géométrique d'une poutre ondulée. (Geometrical
626 homogenization of a corrugated beam). *Comptes rendus de l'Académie des sciences* t314, 425–430
- 627 Radolf, V., Horáček, J., Bula, V., Geneid, A., and Laukkanen, A.-M. (2022). Damping of human vocal fold
628 vibration. In *Engineering Mechanics*, eds. C. Fischer and J. Náprstek. vol. 27-28, 321–324
- 629 Ravanbakhsh, H., Bao, G., Latifi, N., and Mongeau, L. G. (2019). Carbon nanotube composite hydrogels
630 for vocal fold tissue engineering: Biocompatibility, rheology, and porosity. *Materials Science and*
631 *Engineering: C* 103, 109861. doi:<https://doi.org/10.1016/j.msec.2019.109861>
- 632 Rebouah, M. and Chagnon, G. (2014). Permanent set and stress-softening constitutive equation applied to
633 rubber-like materials and soft tissues. *Acta Mechanica* 225, 1685–1698. doi:<https://doi.org/10.1007/s00707-013-1023-y>
- 635 Rebouah, M., Chagnon, G., and Heuillet, P. (2017). Anisotropic viscoelastic models in large deformation
636 for architected membranes. *Mechanics of Time-Dependent Materials* 21, 163–176. doi:<https://doi.org/10.1007/s11043-016-9324-x>
- 638 Roberts, T., Morton, R., and Al-Ali, S. (2011). Microstructure of the vocal fold in elderly humans. *Clinical*
639 *Anatomy* 24, 544–551. doi:10.1002/ca.21114
- 640 Scholp, A., Jeddeloh, C., Tao, C., Liu, X., Dailey, S. H., and Jiang, J. J. (2020). Study of spatiotemporal
641 liquid dynamics in a vibrating vocal fold by using a self-oscillating poroelastic model. *Journal of the*
642 *Acoustical Society of America* 148, 2161–2172
- 643 Shampine, L. F. (2002). Solving $F(t,y(t),y'(t)) = 0$ in Matlab. *Journal of Numerical Mathematics* 10,
644 291–310. doi:10.1515/JNMA.2002.291
- 645 Shen, Z. L., Kahn, H., Ballarini, R., and Eppell, S. J. (2011). Viscoelastic Properties of Isolated Collagen
646 Fibrils. *Biophysical Journal* 100, 3008–3015. doi:10.1016/j.bpj.2011.04.052
- 647 Švec, J. G., Horáček, J., Šram, F., and Veselý, J. (2000). Resonance properties of the vocal folds: in vivo
648 laryngoscopic investigation of the externally excited laryngeal vibrations. *The Journal of the Acoustical*
649 *Society of America* 108, 1397. doi:10.1121/1.1289205
- 650 Tao, C., Jiang, J. J., and Zhang, Y. (2009). A fluid-saturated poroelastic model of the vocal folds with
651 hydrated tissue. *Journal of Biomechanics* 42, 774–780. doi:<https://doi.org/10.1016/j.jbiomech.2008.12.006>
- 653 Tateya, T., Tateya, I., and Bless, D. M. (2006). Collagen subtypes in human vocal folds. *Annals of Otology,*
654 *Rhinology and Laryngology* 115, 469–476. doi:10.1177/000348940611500612
- 655 Terzolo, A., Bailly, L., Orgéas, L., Cochereau, T., and Henrich Bernardoni, N. (2022). A micro-mechanical
656 model for the fibrous tissues of vocal folds. *Journal of the Mechanical Behavior of Biomedical Materials*
657 128, 105118. doi:10.1016/j.jmbbm.2022.105118
- 658 Titze, I. R., Klemuk, S. A., and Gray, S. (2004). Methodology for rheological testing of engineered
659 biomaterials at low audio frequencies. *The Journal of the Acoustical Society of America* 115, 392–401.
660 doi:10.1121/1.1631941
- 661 Vampola, T., Horáček, J., and Klepáček, I. (2016). Computer simulation of mucosal waves on vibrating
662 human vocal folds. *Biocybernetics and Biomedical Engineering* 36, 451–465. doi:10.1016/j.bbe.2016.
663 03.004
- 664 Walimbe, T., Panitch, A., and Sivasankar, P. M. (2017). A review of hyaluronic acid and hyaluronic
665 acid-based hydrogels for vocal fold tissue engineering. *Journal of Voice* 31, 416–423. doi:<https://doi.org/10.1016/j.jvoice.2016.11.014>

- 667 Yang, L. (2008). *Mechanical properties of collagen fibrils and elastic fibers explored by AFM*. Ph.D. thesis,
668 University of Twente, Enschede
- 669 Zhan, L., Qu, S., and Xiao, R. (2024). A review on the mullins effect in tough elastomers and gels. *Acta
670 Mechanica Solida Sinica* 37, 181–214. doi:<https://doi.org/10.1007/s10338-023-00460-6>
- 671 Zhang, K., Siegmund, T., and Chan, R. W. (2006). A constitutive model of the human vocal fold cover
672 for fundamental frequency regulation. *The Journal of the Acoustical Society of America* 119, 1050.
673 doi:10.1121/1.2159433
- 674 Zhang, K., Siegmund, T., and Chan, R. W. (2007). A two-layer composite model of the vocal fold lamina
675 propria for fundamental frequency regulation. *The Journal of the Acoustical Society of America* 122,
676 1090–1101. doi:10.1121/1.2749460
- 677 Zhang, K., Siegmund, T., Chan, R. W., and Fu, M. (2009). Predictions of fundamental frequency changes
678 during phonation based on a biomechanical model of the vocal fold lamina propria. *Journal of Voice :
679 official journal of the Voice Foundation* 23, 282. doi:10.1016/J.JVOICE.2007.09.010

FIGURE CAPTIONS

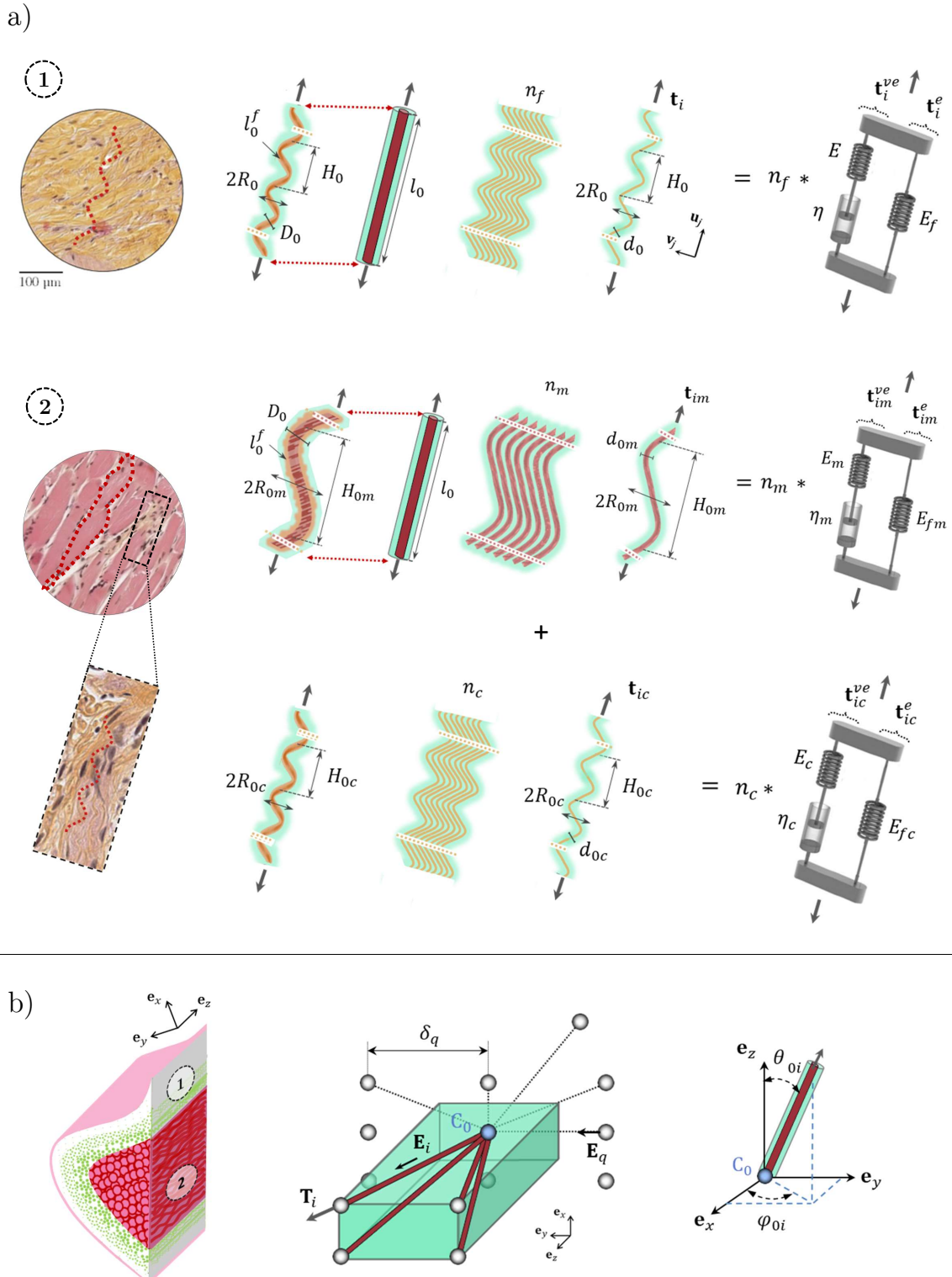


Figure 1. Idealization of the vocal-fold layers. (a) The *lamina propria* ① (resp. the *vocalis* ②) is seen as a network of (orange) collagen fibrils (resp. (pink) myofibrils and collagen fibrils) embedded into a gel-like matrix. Fibrils are self-assembled as collagen fibril bundles (resp. myofibrils surrounded by a sheath of collagen fibrils). Each fibril (and its interaction with its neighboring) behaves as a non-linear visco-hyperelastic Zener model. (b) The fiber bundle microstructure of each layer is seen as a periodic network of 4 orientated fiber bundles (brown) connected at one node C_0 (blue) embedded in a soft isotropic matrix (green). The dotted lines illustrate the 5 possible steric interactions of C_0 with the neighboring nodes. Source: Adapted from Terzolo et al. (2022).

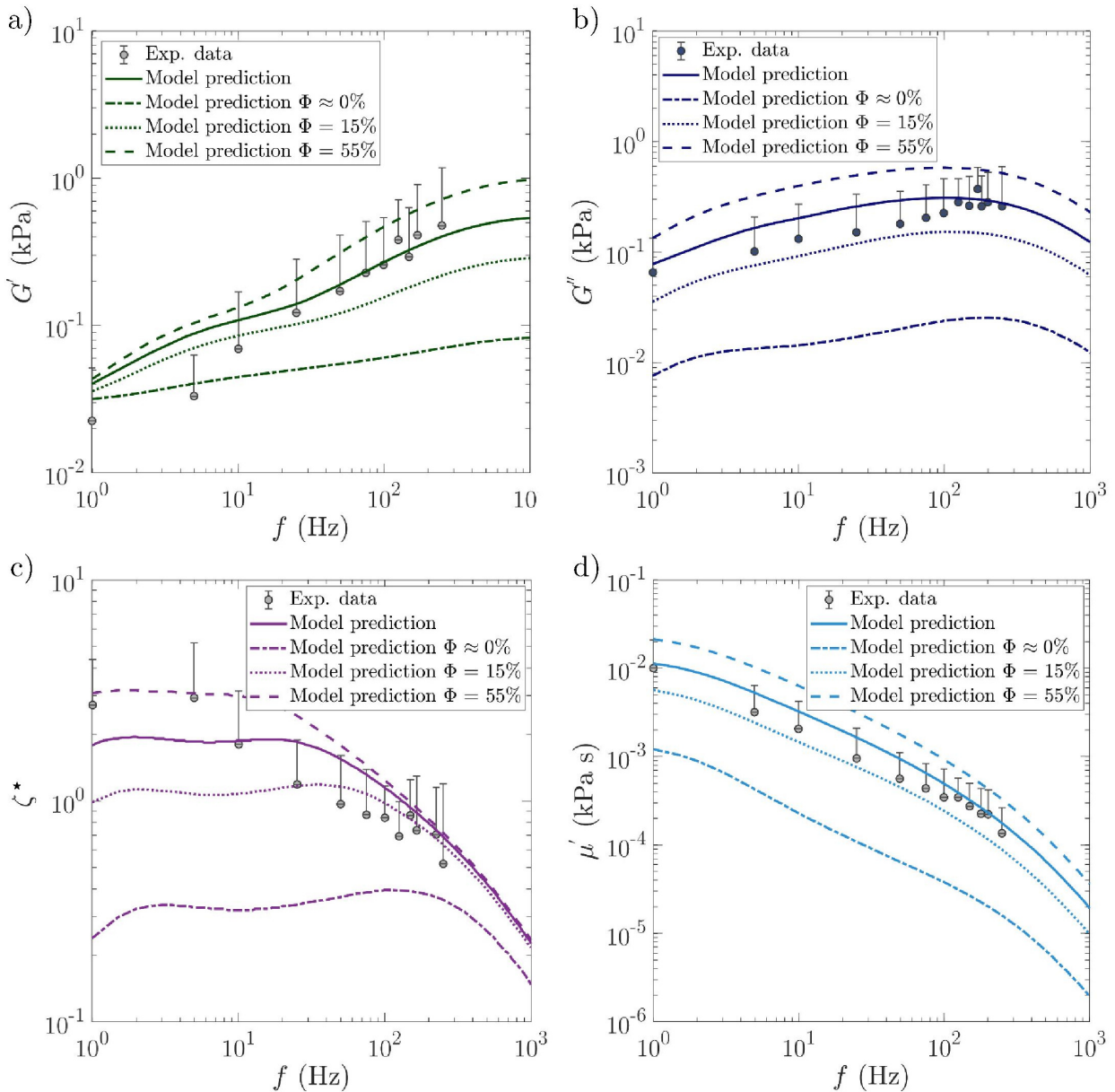


Figure 2. Experimental data (marks) vs. macroscale model predictions (lines) obtained for sample C_{SAOS}: storage G' modulus (a), loss G'' modulus (b), loss factor ζ^* (c) and dynamic viscosity μ' as functions of the oscillation frequency f . The continuous line represents the best fit of the model, the others illustrating the effect of the collagen fibril content Φ . *Source:* experimental data adapted from Chan and Rodriguez (2008). Averaged data and standard deviations from 7 human vocal-fold “cover” specimens are reported.

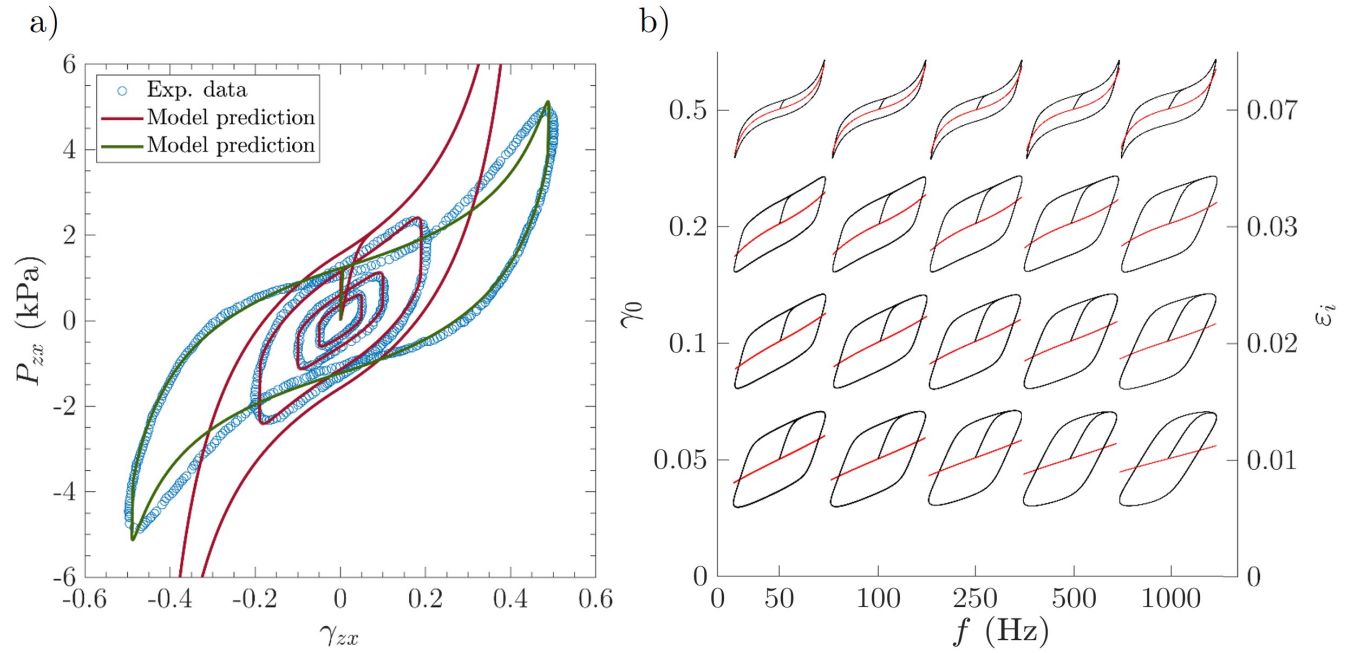


Figure 3. LAOS results : a) Macroscale stress-strain data *vs.* model predictions obtained for sample C_{LAOS} tested at $f = 75$ Hz and with γ_0 varied from 0.05 to 0.5. *Source:* experimental data adapted from Chan (2018). b) Predicted Lissajous stress-strain curves plotted in the Pipkin space $\{f, \gamma_0\}$ or $\{f, \varepsilon_i^{max}\}$, where ε_i^{max} is the maximal cyclic tensile strain the fibrils are subjected to. Black solid lines represent the total stress, while red solid lines are the neutral contribution.

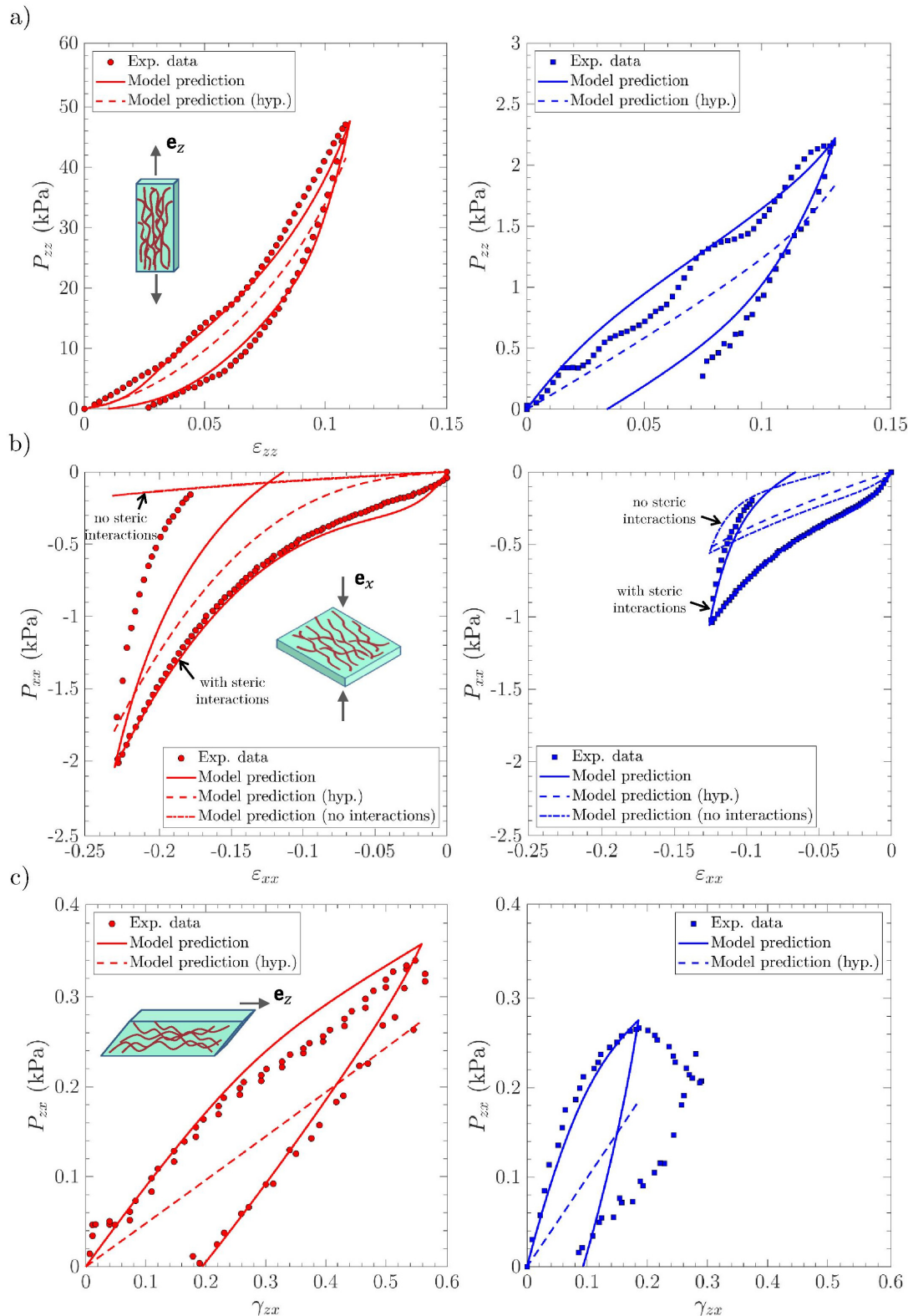


Figure 4. Macroscopic viscoelastic stress-strain curves of vocal-fold sublayers under multiaxial cyclic loadings. Experimental data *vs.* model predictions obtained for *lamina propria* sample LP₁ (*left*, in red) and *vocalis* sample V₁ (*right*, in blue): a) longitudinal tension; b) transverse compression; c) longitudinal shear. Several model predictions are compared: viscohyperelastic model with steric interactions between fibril bundle (*solid lines*); non viscous hyperelastic model previously described in Terzolo et al. (2022) (noted 'hyp.', *dashed lines*). For compression loading solely (panel b), viscohyperelastic model albeit with no steric interactions between fibril bundle (*dashed-dotted lines*).

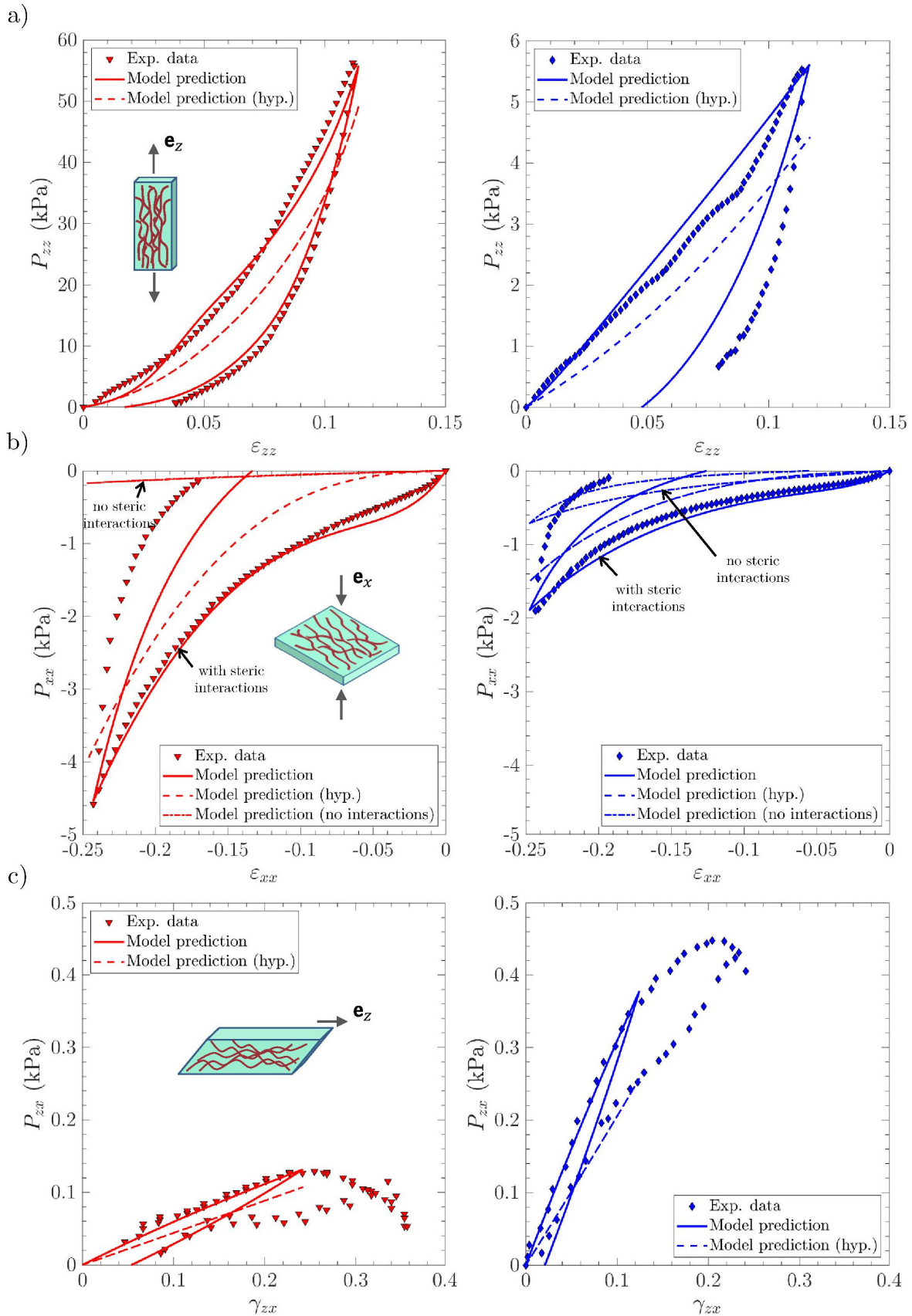


Figure 5. Same as Fig. 4 for samples LP₂ (*left*, in red) and V₂ (*right*, in blue).

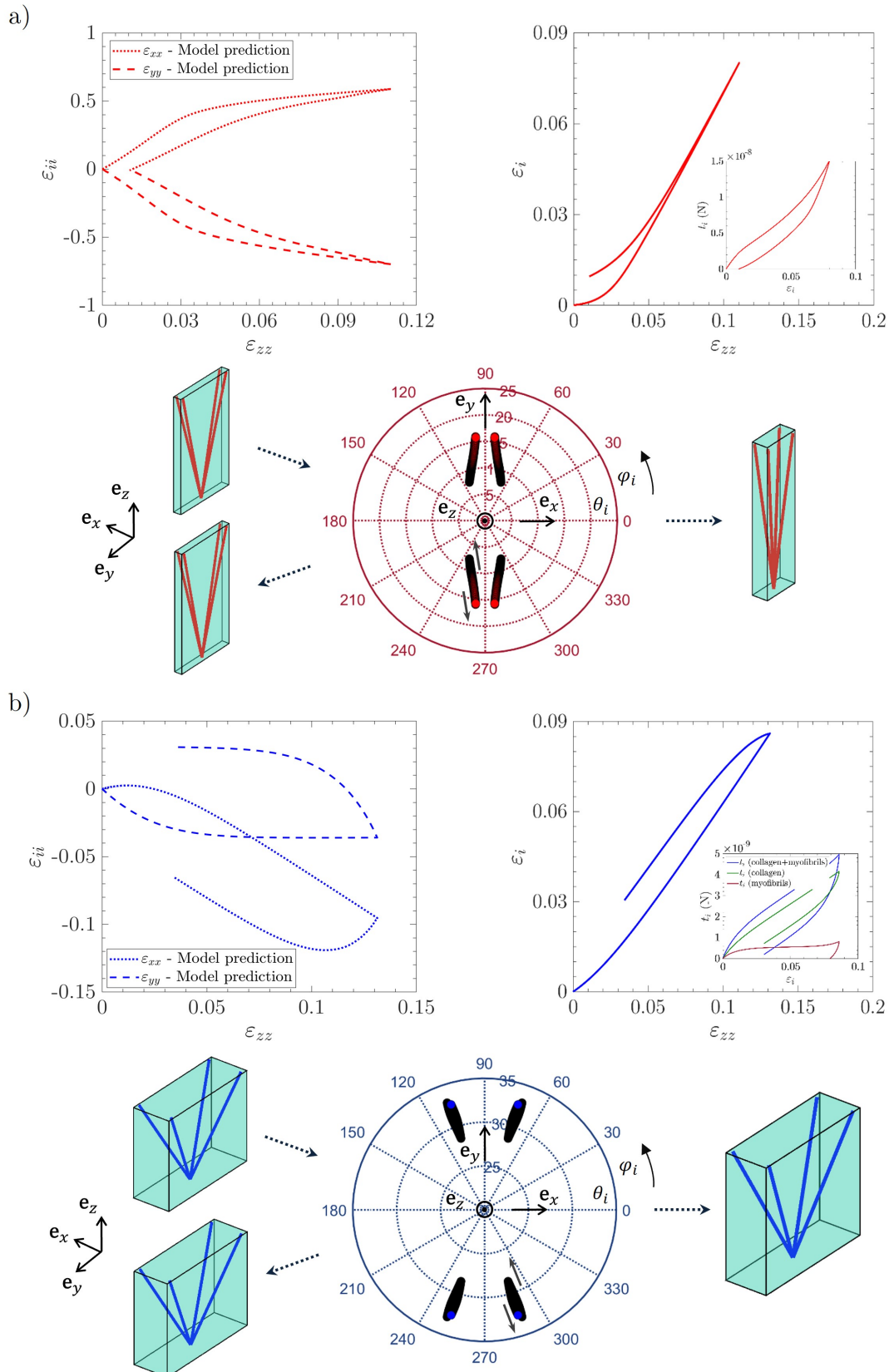


Figure 6. Evolution of multiscale descriptors for *lamina propria* LP1 (a) and *vocalis* V1 (b) during tension along e_z : (top left) macroscopic strain paths; (bottom) stereographic projection of the 4 orientation vectors e_i from initial to final state; (top right) tensile strain of the fibril chord ε_i and corresponding tension t_i .

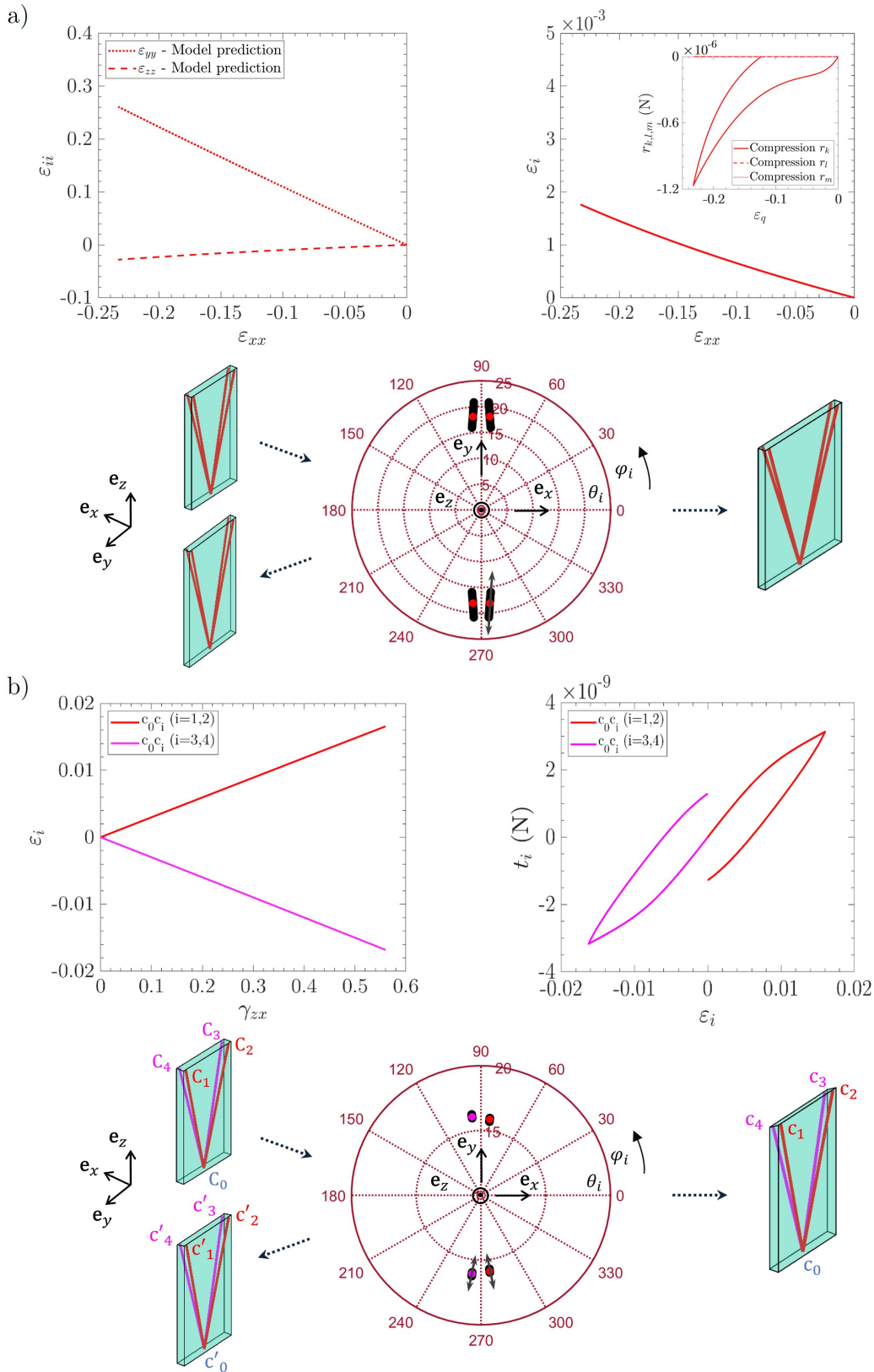


Figure 7. Evolution of multiscale descriptors for *lamina propria* sample LP₁ during compression along e_x (a) and shear in the plane (e_z , e_x) (b). Compression case: (top left) macroscopic strain paths; (bottom) stereographic projection of the 4 orientation vectors e_i from initial to final state; (top right) tensile strain of the fibril chord ε_i and interaction forces R_q . Shear case: (top left) tensile strain of the fibril chord ε_i ; (top right) corresponding tension t_i ; (bottom) same as in (a).

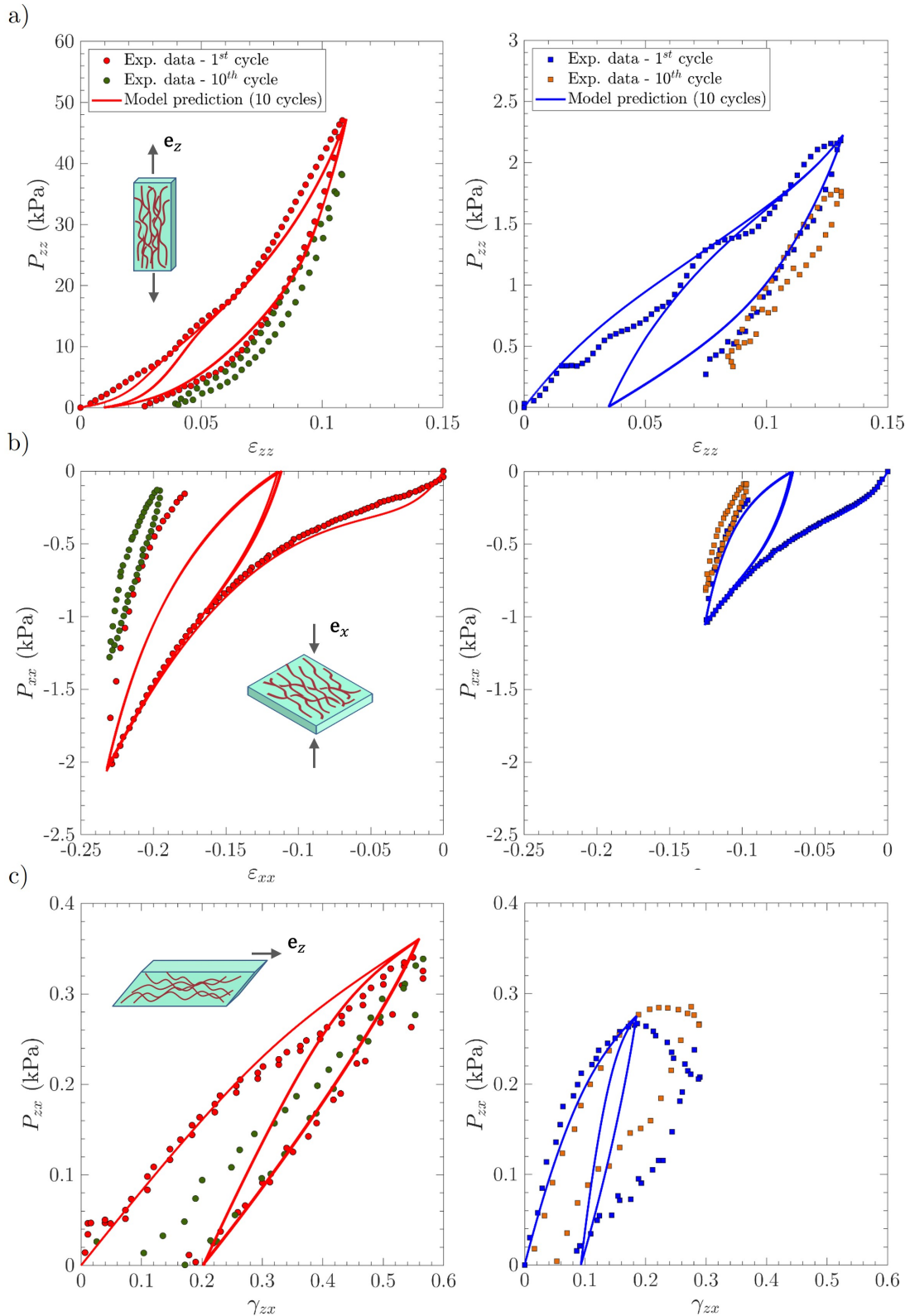


Figure 8. Same as in Fig. 4, albeit for 10 cycles: experimental data vs. model predictions. The experimental 10th cycle is displayed in green symbols for *lamina propria* sample LP₁ (left); in orange symbols for *vocalis* sample V₁ (right). Experimental intermediate cycles are not reported for the sake of clarity.